Properties of Sarychev sulphate aerosols over the Arctic

N.T. O'Neill[1], C. Perro[2], A. Saha[1], G. Lesins[2], T.J. Duck[2], E.W. Eloranta[3], G.J. Nott[2], A. Hoffman[4], M.L. Karumudi[1], C. Ritter[4], A. Bourassa[5], I. Abboud[6], S.A. Carn[7], V. Savastiouk[8]

[1] CARTEL, Université de Sherbrooke, Sherbrooke, Québec, Canada

[2] Department of Physics and Atmospheric Science, Dalhousie University, Halifax, Canada

[3] Space Science and Engineering Center, University of Wisconsin, Madison, USA

[4] Alfred Wegener Institute for Polar and Marine Research, Potsdam, Germany

[5] Institute of Space and Atmospheric Studies, University of Saskatchewan, Saskatoon, Saskatchewan, Canada

[6] Science and Technology Branch, Environment Canada, Wilcox, Saskatchewan, Canada

[7] Department of Geological and Mining Engineering and Sciences, Michigan Technological University, Houghton, USA

[8] Full Spectrum Science Inc., Toronto, Ontario, Canada

Abstract

Aerosols from the Sarychev Peak volcano entered the Arctic region less than a week after the strongest SO_2 eruption on June 15 and 16, 2009 and had, by the second week in July, spread out over the entire Arctic region. These predominantly stratospheric aerosols were determined to be sub-micron in size and inferred to be composed of sulphates produced from the condensation of SO_2 gases emitted during the eruption.

Average (500 nm) Sarychev-induced stratospheric optical depths over the Polar Environmental Atmospheric Research Laboratory (PEARL) at Eureka, Nunavut, Canada were found to be between 0.03 and 0.05 during the months of July and August, 2009. This estimate, derived from sunphotometry and integrated lidar backscatter profiles was consistent with averages derived from lidar estimates over Ny-Ålesund (Spitsbergen). The Sarychev SOD e-folding time at Eureka, deduced from lidar profiles, was found to be approximately 4 months relative to a regression start date of July 27. These profiles initially revealed the presence of multiple Sarychev plumes between the tropopause and about 17 km altitude. After about two months, the complex vertical plume structures had collapsed into fewer, more homogeneous plumes located near the tropopause.

It was found that the noisy character of daytime backscatter returns induced an artifactual minimum in the temporal, pan-Arctic, CALIOP SOD response to Sarychev sulphates. A depolarization ratio discrimination criterion was used to separate the CALIOP stratospheric layer class into a low depolarization subclass which was more representative of Sarychev sulphates.

Post-SAT (post Sarychev Arrival Time) retrievals of the fine mode effective radius ($r_{eff,f}$) and the logarithmic standard deviation for two Eureka sites and Thule, Greenland

were all close to 0.25 μm and 1.6 respectively. The stratospheric analogue to the columnar $r_{eff,f}$ average was estimated to be $r_{eff,f}^{(+)}$ = 0.29 μm for Eureka data. Stratospheric, Raman lidar retrievals at Ny-Ålesund, yielded a post-SAT average of $r_{eff,f}^{(+)}$ = 0.27 μm. These results are ~ 50% larger than the background stratospheric-aerosol value. They are also about a factor of two larger than modeling values used in recent publications or about a factor of five larger in terms of (per particle) backscatter cross section.

1. Introduction

Volcanic eruptions are responsible for the injection of prodigious amounts of primary or secondary aerosols into the troposphere and stratosphere each year. These aerosols take the form of large (generally supermicron) ash particles that disperse across regional scales and small (submicron) sulphate particles that can be dispersed across global scales if the initial injections are stratospheric. The latter particles are formed from gas to particle conversion reactions acting on sulfphur dioxide (SO_2) volcanic emissions. Ash particles typically have a residence time of the order of weeks while sulphate particles are formed in the order of weeks and, if stratospheric, can have a residence times of the order of months (*Bluth et al.*, 1997; *Robock*, 2000).

Robock (2000) points out that the major climatic impact of "explosive volcanic eruptions is through their emission of sulphuric species to the stratosphere, mainly in the form of SO_2 …. These sulfuric species react with OH and H_2O to form H_2SO_4 on a timescale of weeks, and the resulting H_2SO_4 aerosols produce the dominant radiative effect from volcanic eruptions.". However *Kravitz and Robock* (2011) indicated that high

latitude eruptions of moderate magnitude such as the recent Kasatochi and Sarychev eruptions (SO_2 injections ~ 1 Tg) had insignificant radiative effects on a hemispherical global scale. *Haywood et al*. (2010) also argued that eruptions of the magnitude and latitude of Sarychev are not highly significant on a global scale and that observed cooling anomalies in the summer of 2009 could not be unambiguously associated with Sarychev. *Caldeira and Wood* (2008), on the other hand, simulated the more restricted and arguably more critical case of climate change in the Arctic and noted that (climate engineered) mitigation of effects such as the reduction in Arctic ice pack area could be achieved with yearly SO_2 injection rates ~ 0.3 Tg per year: an estimate that is ~ SO_2 mass ejected by volcanos such as Sarychev into the Arctic.

Studies of stratospheric aerosols over the Arctic are understandably driven by particular events, the latest two major events being the Kasatochi and Sarychev eruptions. The former event inspired a series of papers, some of which dealt with the stratospheric aerosol influence over the Arctic: *Hoffman et al*. (2010) employed Raman lidar profiles and sunphotometer measurements to characterize the stratospheric perturbations over Ny-Ålesund, Spitsbergen. *Sioris et al*. (2010) used Measurements of Aerosol Extinction in the Stratosphere and Troposphere Retrieved by Occultation (MAESTRO) data to characterize Kasatochi (autumn) aerosols within an Arctic latitude band of 75-90° N while *Bourassa et al*. (2010) used Optical Spectrograph and InfRared Imaging System (OSIRIS) to extract extinction coefficient profiles across a latitude band of 70-80° N. *Haywood et al*. (2010) and *Kravitz et al*. (2011) carried out global-scale comparisons between modeled Sarychev (sulphate) stratospheric optical depths (SODs) with SODs measured by the OSIRIS sensor: these studies included comparisons in the Arctic.

The June 2009 eruption of Sarychev peak in the Kuril Islands (48.09°N 153.20°E) injected ash and SO_2 gas into the upper troposphere and lower stratosphere. Ash emissions in the Sarychev peak region could be observed from June 12 to June 18 in MODIS imagery. Injection heights were found to vary between 7.5 and 12 km with higher ash clouds from earlier eruptions rising as high as 14 km (estimates from the Global Volcanism Program of the Smithsonian Institution). Stratospheric SO_2 plumes with fine mode particulate plumes in their wake were observed to disperse in a generally easterly direction: modeling simulations supported by satellite data indicated that within about two weeks the particulate matter had circumvented the globe across a latitude range that stretched from near the equator to the high Arctic (*Haywood et al*., 2010). A weak eruption from the Sarychev Peak volcano occurred on June 11, 2009 followed by a series of small eruptions (totaling < 0.1 Tg of SO_2) over the next few days (ibid). The authors pointed out that a significantly larger eruption of 0.5 Tg SO_2 occurred on June 15 followed by an even larger eruption of 0.7 Tg SO_2 on June 16. The latter two days accounted for approximately 86% of the estimated 1.4 ± 0.2 Tg of SO_2 released during the June event. *Haywood et al*. (2010) accordingly modeled Sarychev SO_2 emissions as occurring only on these two days. They assumed SO_2 injection heights to be contained within an altitude range of 11 to 15 km.

In this paper we investigate the effects of the 2009 Sarychev volcanic eruption over the Arctic in order to arrive at a parametric description of the fine mode sulphate particles which, we will argue, were the dominant aerosol influence in the stratosphere, months after the initial eruption. The study will focus on measurements made over the Polar Environmental Atmospheric Research Laboratory (PEARL) in Eureka, Nunavut, Canada

(80.05°N, 86.42°W) and will then broaden to a more pan-Arctic view using satellite data as well as other sources of ground-based data. Due to differing plume transport times to each site, we reference our analysis to pre- and post-Sarychev Arrival Time (denoted as pre-SAT and post-SAT).Various definitions of symbols and acronyms are sprinkled throughout the text that follows: the reader should be aware that all definitions are centralized for easy reference in a Glossary of Symbols and Acronyms.

2. Methodology

2.1. Instrumentation

2.1.1. Ground-based sensors

Our Sarychev analysis was focused on optical measurements acquired using ground-based and satellite based instrumentation. Most of the ground-based measurements were located at PEARL. This high-Arctic observatory is operated as part of the Canadian Network for the Detection of Atmospheric Change (CANDAC). It consists of three measuring sites within a 15 km radius: the Ridge laboratory at 610 meters elevation, the ØPAL (Zero Altitude PEARL Auxiliary Laboratory) about 15 km southeast of the Ridge laboratory, and the SAFIRE (Surface and Atmospheric Flux, Irradiance and Radiation Extension) site about 5 km from ØPAL. Environment Canada maintains a fully equipped meteorological station adjacent to the ØPAL site. Station measurements included vertical profiles of meteorological data obtained from twice-daily radiosonde launches. The PEARL optical instrumentation that we employed, included the CRL (CANDAC Rayleigh-Mie-Raman Lidar) and the AHSRL (Arctic High Spectral Resolution Lidar) at the ØPAL site, two AEROCAN / AERONET sunphotometers / sky radiometers at the

ØPAL and Ridge laboratory and three Brewer SO_2 spectrometers at the Ridge Laboratory.

The AHSRL has been producing 532 nm aerosol backscatter coefficient (β_a) and lidar depolarization ratio (δ_a) profiles at ØPAL since Aug. 1, 2005 [see *Bourdages et al*., (2009) and *Eloranta* et al. (2006) for a discussion of the AHRSL and *Eloranta* (2005) for a general discussion on high spectral resolution lidars]. The CRL measures extinction and backscatter profiles in both the ultraviolet (355/387 nm) and visible (532/607 nm) as well as water vapor at 408 nm, rotational Raman temperatures at 529/531 nm, and depolarization ratio at 532 nm (*Nott et al*., 2011). However, the weak returns from the stratosphere limited analysis to the elastic backscatter channels. Calculation of optical depth from the lidar backscatter profiles thus requires the estimation of a lidar ratio (ratio of extinction to backscatter coefficients) for the stratospheric aerosols. This is discussed in the Processing Considerations section below.

The ØPAL and Ridge Laboratory sunphotometers / sky radiometers are CIMEL instruments associated with the AEROCAN / AERONET networks. Solar extinction measurements permit the retrieval of aerosol optical depth (AOD) across eight spectral channels (340, 380, 440, 550, 670, 870, 1020 and 1640 nm) and at a nominal sampling frequency of once every three minutes (an AEROCAN protocol). This nominal frequency represents an operational maximum : the actual frequency (because of AERONET protocols such as the prohibition of data acquisition in the presence of high humidity and the elimination of low signal / high optical depths) is equal to or less than this value. It also represents a complementary protocol to the nominal AERONET sampling rate of

once every 15 minutes (with a more rapid sampling rate in the presence of large solar air masses).

Combined solar extinction and sky radiance measurements are acquired at a significantly lesser (nominal) sampling frequency of once an hour and are employed in an AERONET inversion algorithm to extract columnar estimates of particle size distribution (PSD) and refractive index (*Dubovik and King,* 2000). The sampling rate is the key to the usage made of the different types of available retrievals; high frequency process studies and comparisons with lidar data are performed using the 3-minute AOD spectra while low frequency analyses of more slowly varying parameters, such as intensive (per particle) properties, are preferentially performed using the more comprehensive AOD and sky radiance inversions. In the "Processing considerations" section below we refer to AERONET inversions and SDA inversions: the former is associated with the low frequency inversions of combined solar extinction and sky radiance measurements while the latter is applied to the high frequency AOD spectra.

The three Brewer spectrophotometers at the Ridge Laboratory collect radiance data at 6 wavelengths in the 300-320 nm region to retrieve columnar abundances of ozone and SO_2. Normally, both direct-sun and zenith sky observations are acquired at Eureka, but only the direct-sun results were used here. Automated measurements of internal mercury and halogen lamps are used in the post-processing chain to compensate for any spectral and radiometric changes in the instrument's characteristics (*Lam et al*., 2007). Advanced analysis for data processing was used (*Savastiouk and McElroy*, 2005) to improve orthogonality between the retrieved ozone and SO_2 vectors.

Ground-based instrumentation outside of Eureka included the Koldewey Aerosol Raman Lidar (KARL) system at Ny-Ålesund. This lidar operates in four elastic backscatter channels at 355, 532 and 1064 nm (parallel and perpendicular polarization at 532 nm) and three inelastic Raman channels at 387, 407, 607 nm (*Hoffman et al*., 2010). AERONET data from the Arctic stations at Thule, Greenland (Denmark) and Hornsund, Spitsbergen (Norway) were employed to analyze retrieval parameters from low frequency AERONET inversions while high frequency AOD data from these two stations and the two CIMELs at Eureka were employed to investigate the information content of AOD spectra versus full-fledged inversions. Data from the Barrow Alaska Arctic station was not used because it was felt that (submicron) tropospheric smoke contamination from Alaskan fires in July and early August engendered AODs that were too elevated and variable.

2.1.2. Satellite-based sensors

The CALIOP lidar aboard the Cloud-Aerosol Lidar and Infrared Pathfinder Satellite Observation (CALIPSO) satellite produces two dimensional "curtains" of backscatter profiles along a polar orbit track which it shares with other sensors in the A-train constellation. The Level 1 output products are linearly polarized, attenuated backscatter coefficient at 532 nm and unpolarized attenuated backscatter coefficient at 1064 nm (*Winker et al*., 2007). The attenuated backscatter profiles are further processed to extract features which in turn are classified into clouds and aerosols and subtypes of clouds and aerosols (ibid). The feature classification allows for the estimation of lidar ratios which in turn permits the transformation of attenuated backscatter profiles to backscatter coefficient and extinction coefficient profiles. In the context of the present paper we note

that in the stratosphere there is no feature sub-classification beyond the assignment of the class “stratospheric layer” (*Liu et al*., 2009).

The OSIRIS instrument aboard the Swedish Odin satellite employs limb radiance measurements of scattered sunlight to retrieve vertical profiles of stratospheric extinction coefficient at 750 nm. The nominal altitude range is 10 to 100 km while the nominal radiance and retrieval resolution is 1 km (*Bourassa et al*., 2007). The actual minimum and maximum altitudes were limited to the estimated height of the thermal tropopause on the lower end and by minimal detectivity constraints on the upper end). The accuracy of retrieved extinction coefficients is ~ 15% in the lower stratosphere (ibid).

The MODIS sensor on the Aqua (A-train) satellite yields multi-band images at a band dependent nadir resolution of 250 to 1000 meters and a cross track swath of 2330 km. Its polar orbit geometry (as for all A-train imagers and profilers) provides a prodigious amount of images / profiles at high-Arctic latitudes. While one can’t use MODIS data for its primary aerosol mandate of estimating AOD (there is no AOD product at high latitudes) we can and frequently do employ MODIS imagery to verify the existence of particular aerosol events (and the fact that the CALIOP tracks run closely to the center of the Aqua image is an extremely useful feature which permits a rudimentary form of 3D monitoring). The OMI (Ozone Monitoring Instrument) on the Aura (A-train) satellite yields estimates of SO_2 columnar abundance (integrated number density) at a nadir resolution of 25 km and a cross track swath of 2200 km (*Krotkov et al*., 2006).

2.2. Processing considerations

2.2.1. Derivation of SODs

If one accepts the premise that stratospheric aerosols were dominated by Sarychev fine-mode sulphates for the post-SAT period then we have every interest in trying to characterize the intrinsic properties of these aerosols. In order to employ the lidar ratio to transform lidar backscatter coefficients to extinction coefficient profiles and then SODs [see *Weitkamp* (2005), for example], transform extinction coefficients or optical depths from one wavelength to another, or extract a value of fine-mode effective radius from its Van de Hulst analogue (*O'Neill et al*., 2008a), one needs to establish a nominal particle PSD and nominal refractive index. The overreaching premise of dominance by fine mode sulphate aerosols during the Sarychev period is established circumstantially below by demonstrating that the plumes over Eureka and over a pan-Arctic scale were composed of fine mode, low depolarization particles with linkages to SO_2 incursions over the site (and, again, over a pan-Arctic scale) as well as by the general observation, based on evidence such as backtrajectories and satellite data, that a strong stable influx of fine mode stratospheric aerosols must have been associated with the Sarychev eruption.

Table 1 shows the parametric values used to represent these particles along with technical details and citations. The fine mode PSD was modeled as a log-normal distribution whose parameters (σ_f and $r_{eff,f}$) were extracted from post-SAT averages of fine mode AERONET inversions applied to AODs and sky radiance data from the ØPAL site. These two parameters are determined as part of the AERONET Version 2 product output by applying first-principle definitions to the generalized PSD retrievals (details on these retrievals as well as how the refractive index of Table 1 was established can be

found below in the "AERONET inversion" section). Once the parameters of the fine mode PSD and the refractive index had been defined, the lidar ratio and the wavelength transformation factors of Table 1 were computed from a Mie code. An analysis of the variation of the nominal Table 1 values is given in the "AERONET retrievals" section below.

SOD estimates were obtained for CRL, AHSRL and CALIOP backscatter profiles using the lidar ratio of 59 sr given in Table 1 and integrating the resulting extinction coefficient profiles from the tropopause (determined from EC radiosonde data) to the highest profile altitude. In the case of the AHSRL data the retrieval of β_a means a decoupling of aerosol and Rayleigh contributions using high resolution Doppler spectrometry followed by the application of the lidar ratio of Table 1 to the resulting aerosol backscatter coefficients while in the case of the CRL and CALIOP profiles this means the solution of the lidar equation supposing the same lidar ratio. An estimate of the SOD contribution due to Sarychev sulphates was defined as

$$\Delta SOD = SOD - \langle SOD \rangle_{pre\text{-}SAT} \quad (1)$$

where the latter term represents an average of pre-SAT SODs (i.e. the stratospheric aerosol background).

AERONET inversions applied to (low frequency) solar extinction / sky radiometry data as well as simpler inversions applied to (high frequency) AOD spectra yield an estimate of the fine mode optical depth at 500 nm (τ_f), the columnar contribution of sub-micron particles to the AOD (see the inversion section below). Since, as will be seen, Sarychev sulphates are fine mode, the difference $\Delta\tau_f$ defined as

$$\Delta\tau_f = \tau_{f,\,post\text{-}SAT} - \langle \tau_{f,\,pre\text{-}SAT} \rangle \quad (2a)$$

represents the change induced by the advent of the Sarychev plumes over the Arctic or, given that these plumes were largely stratospheric, an estimate of ΔSOD,

$$\Delta SOD \sim \Delta\tau_f \qquad (2b)$$

For our analysis of Eureka SODs, OSIRIS extinction coefficient profiles within approximately 270 km of the site were integrated from approximately the height of the thermal tropopause to the maximum stratospheric height at which the extinction coefficient measurements were judged to be significant. While the ability to retrieve extinction coefficients at 750 nm is a valuable feature (i.e. unlike lidar backscatter coefficients, there is not a strong dependency on the scattering phase function, or more specifically, the lidar ratio), the transformation to our wavelength standard of 500 nm requires one to assume a PSD and refractive index to represent the Sarychev stratospheric sulphate aerosols (i.e. in order to estimate the $(C_{ext}(500) / C_{ext}(750)$ factor of Table 1). The impact of such assumptions is discussed below.

2.2.2. e-folding times

It is a trivial matter to show that if the SOD temporal behavior can be approximated as SOD(t) = a exp(-bt) then the e-folding time [the time over which the SOD is reduced by a factor of 1 / e from a reference value of $SOD(t_0)$] is independent of t_0 and a,

$$\Delta t_{1/e} = t(SOD(t_0) / e) - t_0$$

$$= 1 / b \qquad (3)$$

However if the SOD temporal behavior is something less than exponential over segments of the time range then there is t_0 dependency inasmuch as the regression value of "b" will be affected by the selected starting point of the exponential regression (as well as the end point) for seasonally restricted sensors such as OSIRIS.

2.2.3. AERONET inversions

Low frequency AERONET Level 1.5 (Version 2.0) PSD and refractive index inversions for Eureka ØPAL data were employed to fix the optical and microphysical values to the nominal stratospheric sulphate parameters of Table 1 (the use of Level 1.5 inversions rather than quality-assured Level 2.0 inversions was necessitated by the fact that there were few or no inversions in the Level 2.0 category). Although inversions from the other Arctic or sub-Arctic AEROCAN / AERONET sites were available, we focused the Table 1 characterization of Sarychev sulphate properties on Eureka: this was motivated by the fact that the AHSRL profiles gave us objective and fairly continuous proof that τ_f variations were dominated by Sarychev plumes. In retrospect, the early focus on Eureka in establishing the Table 1 parameters was probably unnecessary since the retrievals from the other Arctic stations gave substantially the same results (see below). The fine mode / coarse mode separation of the total retrieved PSD is defined relative to the minimum of the volumetric PSD (dV / dln r) for Version 2.0 retrievals (*Anon*, 2006). This enables the computation of the fine mode microphysical parameters defined in Table 1 (notably $r_{eff,f}$) and subsequently the estimation of τ_f at 500 nm.

2.2.4. SDA inversions

High frequency (3 minute) sunphotometer AOD spectra were also processed using the SDA (Spectral Deconvolution Algorithm) and FMC (Fine Mode Curvature) algorithm to subdivide the AOD into total, fine and coarse mode ODs (τ_a, τ_f and τ_c) at 500 nm and to retrieve an estimate of $r_{eff,f}$ (*O'Neill et al.*, 2003; *O'Neill et al.*, 2008a). These simpler but robust inversion products, with the exception of $r_{eff,f}$, are also available on the AERONET web site. We employed (a) Level 1.0 ("raw") AOD data for high frequency τ_f

comparisons with AHSRL profiles and (b) Level 2.0 (cloud-screened and quality assured) AOD data for lower frequency comparisons with τ_f and $r_{eff,f}$ results from full-fledged AERONET inversions.

2.2.5. Lidar (KARL) inversions

Lidar inversions for particle size and refractive index were performed on specific days using the multi-band retrieval algorithm of *Hoffman et al*. (2010). This technique employs β_a from the 355, 532 and 1064 nm elastic channels of the KARL lidar along with estimates of the aerosol extinction coefficient derived for the 355 and 532 nm channels to retrieve estimates of the refractive index and the fine mode volume size distribution. The β_a values are derived from backscatter ratio (β_a / $\beta_{molecular}$) estimates, where normalization is performed using inelastic channels, while the extinction coefficient estimates depend on altitude derivatives of an inelastic channel: both types of estimates suffer from the weak signal to noise of the inelastic channels and thus require the presence of a strong plume event and significant (noise reducing) averaging in the horizontal direction. KARL data were processed with a spatial and temporal resolution of 30 m and 30 minutes. The extinction coefficient estimates were then averaged over vertical layers identified as being associated with Sarychev aserosols. This yielded an effective vertical resolution ~ 150 m.

3. Sarychev aerosols over Eureka

3.1. SOD Illustrative case study

Figure 1 shows an illustration of Sarychev plume data acquired over Eureka on July 1 and 2, 2009. These two days were particularly interesting because the rapidly decaying

SO_2 abundance was still relatively strong while the plume was of sufficient strength that backscattering effects could be seen in MODIS data. Figures 1(a) and 1(b) show AHSRL aerosol β_a and δ_a profiles respectively. The vertical banding evident in these profiles are artifacts due to degrading instrument performance (at the time of these measurements, the AHSRL was due for a maintenance overhaul). We should also note that the bright vertical streaks above strong backscatter features (notably the clouds found below the tropopause after 1800 UT on July 2) are probably the result of detector afterpulsing generated by the detectors being exposed to large backscatter signals.

In Figures 1(a) and (b) the radiosonde-derived tropopause is marked as a purple line. The volcanic aerosol plumes above the tropopause are distinguishable from the cirrus clouds below the tropopause by significantly lower depolarization ratio (a signature difference between submicron aerosols and supermicron, irregular-shaped crystals). Fig. 1(c) shows the result of deconvolving AOD spectra from the ØPAL sunphotometer (i.e. applying the SDA algorithm) into total, fine and coarse mode components at 500 nm (τ_a, τ_f and τ_c in black, red and blue) along with SODs computed by integrating the AHSRL backscatter coefficient profiles from the tropopause to just above the highest observable plume (using the lidar ratio of Table 1 and converting to 500 nm). The correlation between the AHSRL SODs of low depolarization ratio and τ_f is consistent with the typically strong correlation that we have seen in the past for fine mode smoke events (*Saha et al*., 2010; *O'Neill et al*., 2008b). Certain high frequency departures from the relatively lower frequency behavior of the τ_f curve are clearly artifactual in nature and related to the banding effect seen in the lidar data. We would also note that the high values of τ_f in Fig. 1(c) are rather unique: no other post-SAT measurements of τ_f at

Eureka were greater than 0.2. Figure S1 of the auxiliary material shows a series of 5 Terra images acquired over Eureka around the (July 1) τ_f peak of Fig. 1. These images show what appears to rather dispersed and nearly sub-visual plume whose radiance variation over Eureka was nonetheless qualitatively coherent with the τ_f variations of Fig. 1.

The positive correlation between τ_f and the three Brewer SO_2 abundances [Fig. 1(d)] supports the general affirmation that the τ_f values are associated with particulate byproducts of SO_2 condensation. This type of positive correlation is qualitatively supported in a spatial sense by the July 1 and July 2 OMI-SO_2 and CALIOP-SOD images seen in Fig. 2. One can note a degree of spatial correspondence over Eureka on both days and as far south as Baffin Island on July 2. This affirmation must obviously be tempered by the knowledge that such a comparison is fraught with a variety of orbit and environmentally induced sampling problems in the OMI and CALIOP data (not to mention the fact that the conversion from SO_2 gas to sulphate particles is an essentially anti-correlative process). These sampling problems represent a particular challenge in the latter case: aside from the obvious limitation of having no profiles above the CALIPSO orbit limit of 82° N latitude (indicated by a white semi-circle on the July 1 CALIOP image), one often encounters sparse and irregular sampling patterns (the triangular artifact at the bottom of the July 2 CALIOP image, for example).

3.2. Independent lidar ratio estimates from the AHSRL profiles of July 1 and 2

AHSRL profiles can be used to directly estimate the optical depth and the lidar ratio of a volcanic aerosol layer: the former is derived from the extinction of the molecular signal by the aerosol layer, while the latter is retrieved from the ratio of this optical depth

to the vertically integrated β_a profile (*Sroga et al*., 1983). Time averaging is required to extract optical depths from the weak molecular signals. We derived optical depths and lidar ratios across strongly backscattering layers between 10 and 15 km for the periods ranging from 19:55 to 20:10 UT (the sharp July 1 peak of Fig. 1) as well as 21:10 to 21:59 UT on July 1 and 05:35 to 06:39 on July 2. The July 1 periods yielded optical depths of 0.4 and 0.08 with lidar ratios of 51 and 59 sr respectively, while the July 2 case provided an optical depth of 0.085 and a lidar ratio of 55 sr. These measured lidar ratios are in reasonable agreement with the (AERONET inversion) derived value of 59 sr employed in Table 1 (that value differs by less than 10% from the mean of the three AHSRL-derived values).

4. Temporal evolution of Sarychev aerosols in the Arctic

4.1. SOD

4.1.1. Temporal evolution – Eureka

Fig. 3 shows a temporal plot of estimated (500 nm) SOD over Eureka as measured by the AHSRL, the CRL, and OSIRIS as well as τ_f from the ØPAL sunphotometer. A sharp increase (except for the CRL which was not operating at the time) follows the SAT of June 25 (black dashed vertical line). The τ_f values from the sunphotometer are significantly greater than the lidar and OSIRIS SODs because they include the optical effects of the troposphere. OSIRIS SODs appear to be substantially less than the SODs derived from the lidar backscattering profiles: the discussion of this discrepancy is deferred until the SOD statistical section below. One can also observe that the lidar SOD

amplitudes had descended to near background values around Feb. of 2010, approximately 6 months after the SAT.

4.1.2. Temporal evolution – pan-Arctic

A close scrutiny of CALIOP profiles showed that significant, low depolarization SODs entered the Arctic during the week of June 16 to 20 from the Russian Arctic and Alaska. The pan-Arctic CALIOP SOD (5-day average) frames of Fig. 4 show this initial incursion and suggest that advective circulation had rendered the influence of these stratospheric aerosols essentially circumpolar by the first week of July (the apparent "black hole" in the CALIOP frames of Fig. 4, south of the orbital limitation of 82° N, is dealt with below). Animation A1 of the dynamic content shows the evolution of OMI SO_2 abundances across the Arctic: it is instructive to play this animation alongside the SOD mosaic of Fig. 4.

4.1.2.1. Sub-classification of CALIOP's "stratospheric layer" class

It was pointed out above that the CALIOP processing does not perform any sub classification of the class "stratospheric layer": this means that thin-layer clouds can and do contribute to the SODs extracted from CALIOP data (PSCs in the winter and near-tropopause clouds in the summer: the latter may well be more a result of CALIOP vertical resolution ambiguity and/or uncertainty in the position of the tropopause). In order to increase the probability that CALIOP SOD estimates were confined to sub-micron sized particles we employed the CALIOP δ_a value associated with the stratospheric layer class. Visual observations of obvious Sarychev plumes and clouds associated with that class enabled us to arrive at a primitive sub-classification scheme: division of these layers into $0 < \delta_a \leq 0.2$ and $\delta_a > 0.2$ sub-classes permitted a degree of

separability according to our case study analysis. These low and high δ_a subclasses could then be linked to more appropriate lidar ratio values: the sulphate lidar ratio of Table 1 for the low δ_a case and the standard stratospheric lidar ratio of 25 sr for the high δ_a case (the latter lidar ratio being associated with stratospheric layer class in the CALIOP processing chain, a value that is meant to be typical of cloud: see Table 4.1 of *Vaughan et al*. (2005) for example).

4.1.2.2. Pan-Arctic sub-classification results

Fig. 5(b) shows the temporal variation of CALIOP SODs that have been spatially averaged across the Polar cap north of the Arctic Circle (specifically, all non-zero optical depths of the stratospheric layer class on a given day and within the Arctic Circle were arithmetically averaged). The black circular symbols are daily averages without δ_a sub-classification (but converted from the nominal CALIOP lidar ratio of 25 to the Table 1 lidar ratio of 59 sr). The red and blue segmented curves correspond to 10 day averages of the CALIOP SODs that have been segregated into the low and high δ_a sub-classes while the black segmented curve is the (sample weighted) combination of these two classes with their different lidar ratios. Ten-day averaging was felt to be appropriate given the sparseness of SOD samples in the pre-SAT period: this is evident in Fig. 5(a) where the number of samples employed in the 10 day averages is sometimes in the hundreds (spread across the Arctic). Indeed Fig. 5(a) shows few low δ_a samples during the pre-SAT period with SODs being dominated by high δ_a events [except during the period from early to mid-April, approximately Day of Year (DOY) 100 to 120 when, the Redoubt volcano in Alaska was particularly active]. The post-SAT SODs, are dominated by low δ_a samples: this Arctic-wide observation is coherent with our supposition (supported by

Eureka AHSRL data) that Sarychev aerosols were characterized by low depolarization. The plots of sample number combined with the SOD plots of Fig. 5(b) tell us at least two things: that low δ_a ratio statistics during the pre-SAT phase are probably unreliable and that one could have ignored our sub-classification protocol in the post-SAT phase (i.e. the SOD daily average and the low δ_a SODs roughly match in the latter case). In Text S1 of the auxiliary material (Section 1) we give an illustration of the instability of pre-SAT, low δ_a SODs and how changing the δ_a threshold from 0.2 to 0.1 only affects pre-SAT statistics.

The Arctic-averaged, OMI-SO_2 abundances of Fig. 5(b) (grey symbols), show dramatic differences in residence time of sulphates and SO_2. While the former is of the order of months, the SO_2 abundance was significantly above background levels for only about 3½ weeks (DOY 169 to 193 or June 18 to July 12). It is curious that the SO_2 abundances share an apparent anomaly with the low δ_a SODs inasmuch as the pre-SAT values are higher than post-SAT values (well removed from the initial peaking); however for the reasons given above, we do not have a lot of confidence in the pre-SAT values of low δ_a SOD.

In Fig. 5(c) we compare OSIRIS SOD retrievals at 500 nm to the low depolarization CALIOP curve of Fig. 5(b). The OSIRIS SODs were first averaged over the latitude region between 70° and 80° N and then averaged over the same 10-day bins employed for the CALIOP data. One can observe the same SOD peak near the end of July as noted by *Haywood et al*. (2010) in the case of a latitude band around 80° N. The possible reasons for the lower OSIRIS SODs are discussed in the SOD summary statistics section.

4.1.2.3. Apparent "sulphate hole" in pan-Arctic, CALIOP SODs

The Fig. 5(b) minima in the CALIOP SOD curves at around day 220 (Aug. 8) merit particular attention. The small dark hole evident in Fig. 4 at the beginning of the frame series is associated with the 82° latitudinal sampling limit of CALIOP. However, one can also observe an apparently expanding and then contracting circle of weak SOD values which reaches a maximum in size around Aug. 6 -10 (day 218 to 222) and returns to the latitudinal diameter of the CALIOP sampling limit at the end of September.

A case-study survey of daily-averaged Polar SOD images and individual CALIOP profiles showed that the majority of samples classified as SODs by the CALIOP feature identification algorithm correspond to nighttime data (a not unexpected result given the clearly superior signal to noise character of nighttime vs daytime profiles: see Fig. S2a and S2b of the auxiliary material for an illustrative example). This means that SODs extracted during the daytime will be noisier (more isolated) and optically thinner than those acquired during the night. The decrease in the size of the "dark holes" after Aug. 8 in Fig. 4 is likely associated with the size of the latitude circle of 24 hour sunlight given by $\lambda = \pi / 2 - \delta$ (where δ is the positive solar declination angle between the spring and fall equinox: correspondingly, $\lambda = \pi / 2 + \delta$ indicates the latitude of 24 hour darkness where δ is the negative declination between the fall and spring equinox). This circle of 24 hour sunlight (whose general influence, in terms of being associated with predominantly sunlit conditions extends beyond its immediate borders) corresponds to a (maximal) latitude circle that lies just above the Arctic Circle at the time of the summer solstice (June 21) and shrinks to zero at the spring and fall equinoxes (Mar. 21 and Sept. 22 respectively). These dates are superimposed on the CALIOP SOD plot in Fig. S2c of the

auxiliary material. The noise effect of the maximal sunlit area at the summer solstice is however offset by the very strong SODs just after the arrival of the plumes in the Arctic: in this case the Sarychev optical signal was strong enough to ensure a competitive number of samples being classified as SODs during the daytime. The net result of these competing influences (decreasing SOD and decreasing daylight influence with time) is the "sinc" function shape evident in the SOD temporal plot of Fig. 5(b) [as well as the minimum in the number of low depolarization samples seen in Fig. 5(a)].

4.1.3. SOD Statistical summary

4.1.3.1 SOD and ΔSOD amplitudes for Eureka and the Arctic region

The first three groupings of multi-colored columns in Figure 6(a) shows the summary optical depth statistics for the sunphotometer, the AHSRL, OSIRIS and the CRL at Eureka averaged over a pre-SAT period (May 1 to June 24, labeled "Background") and the months of July and August (labeled "no background subtraction"). The July averages for this particular graph exclude the data of July 1 and July 2 in the cases of the sunphotometry and the AHSRL because it was determined that measured optical depths on these two days were too variable (significant numbers of points on these two days were beyond the 3 x standard deviation distance usually taken as the definition of an outlier). The error bars of Fig. 6 represent the standard deviation over the populations of points employed in determining these averages. The derived τ_f values for the sunphotometry include the tropospheric column so they are significantly larger than the SOD values: the differently tinted red colored columns indicate the difference between the regular AERONET inversion and the SDA retrieval: at least part of these systematic differences could well be due to a difference in definition of τ_f (*O'Neill et al.*, 2003).

The fourth and fifth groupings of multi-colored columns show ΔSOD as defined in equations (1) and (2) averaged over July and August. The averaged ΔSOD values from the AHSRL and the sunphotometry are in moderately good agreement in July and August (roughly 0.03 and 0.05 respectively for both months). In spite of the large standard deviations, it is interesting to observe that the "common mode" differences between the sunphotometer τ_f estimates largely disappear in the ΔSOD results. *Kravitz et al*. (2011) reported KARL derived values of 0.045 and 0.036 as average SODs at 532 nm for the month of July and August at Ny-Ålesund (estimated lidar ratio of 50 sr). With an estimated pre-Sarychev (May and June) average of 0.0072 this yields ΔSOD values of 0.038 and 0.029 at Ny-Ålesund (their table indicates 0.0072 at 750 nm whereas it should have indicted 0.00216 or hence, 0.0072 at 532 nm using their 750 nm to 532 nm transformation factor of 0.3). This is within the error margins of the Eureka AHSRL results for July but not August. We note however that the AHSRL results in August represent a poor sampling: the problems with the AHSRL during that month were particularly egregious with only 7 days out of 31 showing substantial stratospheric profiles (there was, notably, no data after Aug. 19).

The OSIRIS values of ΔSOD are somewhat lower (approximately half of the AHSRL estimates). The agreement does improve if one uses the simple expedient of employing the smaller prescribed Sarychev $r_{eff,f}$ values of *Haywood et al*. (2010) to make the transformation from the OSIRIS SODs at 750 nm to our standard at 500 nm. However we can eliminate the sulphate model dependency by computing ΔSOD at 750 nm for the sunphotometer data: the result shows that OSIRIS ΔSOD remains significantly below the sunphotometer value of ΔSOD (by more than a factor of 2 for July and August data

respectively). In Text S1 of the auxiliary material (Section 2) we discuss how OSIRIS extinction coefficient profiles undergo (a) a general vertical filtering effect which apparently reduces the profiles to low frequency representations of the high frequency AHSRL profiles and (b) a systematic reduction in the amplitude of the OSIRIS extinction profiles and computed SODs relative to the AHSRL results. While field of view (FOV) averaging effects would appear to be the cause of the low frequency filtering, the reasons for the systematic reduction in amplitude are not evident in these comparisons.

Figure 6(b) shows the equivalent set of statistics for pan-Arctic estimates of SOD and ΔSOD from CALIOP and OSIRIS. The CALIOP results represent the averages of the red ($\delta_a \leq 0.2$) 10-day averages shown in Fig. 5(b). The pre-SAT averages were taken from May 1 to June 19, 2009 (where the latter date was derived from a detailed assessment of CALIOP SOD images). The CALIOP pre-SAT SODs are significantly larger than the OSIRIS SODs as are the July SODs. The ΔSOD values, because of the large pre-SAT values are negative for CALIOP in August [as is evident in Fig. 5(b)]. For reasons given above in the discussion surrounding Fig. 5(a) and 5(b) we do not have high confidence in the CALIOP pre-SAT SODs and accordingly feel that they have an important role in the production of negative ΔSOD values in August. The OSIRIS ΔSOD values are about half of the OSIRIS Eureka values for Fig. 6(a) (about 0.01 versus 0.02). Aside from possible regional differences between pan-Arctic averages and the Eureka results, the pan-Arctic averages were computed above the 380 °K potential temperature level rather than the thermal tropopause (as per *Bourassa et al.*, 2010: the 380 °K potential temperature level is typically used to indicate the top of the tropical tropopause layer and represents a natural flow pathway from lower to higher latitudes). This altitude was typically ~ 13 km

and thus would be expected to produce smaller amplitude estimates of SOD and ΔSOD than the Eureka estimates that were based on vertical integrations using the thermal tropopause as the lower limit (versus typical thermal tropopause altitudes <~ 10 km as per Fig. 7).

4.1.3.2 E-folding times

Table 3 shows e-folding times calculated in this study along with Sarychev e-folding times computed by *Haywood et al*. (2010) and *Kravitz et al*. (2011) using ORISIS data acquired across high latitude bands. All e-folding times were computed using equation (3) applied to exponentially regressed SODs (or ΔSODs in the case of *Haywood et al*. (2010)) with a t_0 of July 27, 2009. This value corresponds to an apparent peak in their OSIRIS data but which is not evident in AHSRL and sunphotometry data. This particular peak day was observed by *Haywood et al*. (2010) after applying time-bin filtering to their OSIRIS ΔSOD plots and appears to be close to the peaks that one would obtain by fitting a low order polynomial to the OSIRIS data of *Kravitz et al*. (2011) and to the OSIRIS data employed in this study (it does vary with the type of low order fit applied but for the sake of having a standard regression start time we chose July 27). In general one can note that the AHSRL / CRL e-folding time is about a month greater than the e-folding time of the near-Eureka OSIRIS case and that the latter is about a month less than the e-folding time that we computed for the OSIRIS, pan-Arctic (70° – 80° N) average. This latter case is about a month greater than the time computed by *Kravitz et al*. (2011) for the same data set and about two months greater than the e-folding time of *Haywood et al*. (2010) for a pan-Arctic OSIRIS average about an 80° N band.

Of these diverse e-folding time estimates we would tend to have more confidence in the lidar-derived (Eureka) values since different cutoff dates in SOD data near the middle to the end of October (the limitation of OSIRIS data) can produce significant increases in OSIRIS derived e-folding times (a week or two reduction in the October cutoff time of the OSIRIS near-Eureka case causes the e-folding time estimate to increase by ~ a month: the reason for this increase can be qualitatively seen in Fig. 3 where the OSIRIS SODs decay rapidly near the beginning of October). In contrast the time range of lidar SOD samples extended to February of 2010 and accordingly generated more robust estimates of e-folding time (again, the reader should refer to Fig. 3 to appreciate this). The smaller e-folding times for the ΔSOD regressions of *Haywood et al*. (2010) must in part be due to the fact that such a regression will be dependent on the background SOD that is subtracted to compute ΔSOD and will have a tendency to increase the exponential regression slope (decrease the e-folding time) relative to an SOD exponential regression. The only reason we can offer for the 70° – 80° N discrepancy of the last column in Table 3 are computational differences: for example, *Kravitz et al*. (2011) did not specify what their value of t_0 was (we get about the same results as they do if we increase our t_0 value by about 2½ weeks).

4.2. Sulphate plume height

Figure 7 shows the temporal evolution of Sarychev plume heights and the height of the tropopause over Eureka. The colored circles show the altitude of the plume of maximum backscatter while the grey area represents the range of altitudes over which a plume was detected (i.e. in the case of multiple overhead plumes or one or two thick plumes as occurred in the latter part of the sampling period). These plumes were visually

characterized (across the span of a day) from the AHSRL and CRL backscatter profiles; while the maximum backscatter altitude is a fairly objective measure, the estimation of the range of plume heights was more subjective and a degree of ambiguity could exist in determining the extent of the grey zone (a case in point is the illustration of Fig. 1(a): near the end of July 2 there is a complicated structure involving multiple plumes, and, possibly false positives where the backscatter is relatively weak.

Plumes were assumed to be Sarychev sulphate aerosols if they were distinct backscatter plumes seen by the AHSRL or the CRL and if they were above the tropopause. Wherever possible, the backscatter evidence was supported by evidence of (a) low δ_a (a necessary but not sufficient condition for the plumes being composed of sub-micron aerosols: see *O'Neill et al.*, 2008b for example), (b) associated τ_f variation from the sunphotometry and (c) backtrajectories that could be traced back to the eruption coordinates. Fig. 1(a) and 1(b) illustrate well the presence of high-backscatter, low depolarization stratospheric plumes. The supporting evidence was not always available (depolarization data were not available for the CRL during this period or backtrajectories to the Sarychev peak became indeterminate as the plumes aged and became well mixed).

The general decrease of plume height with time, after an apparent increase in plume height until about mid-July, is evident in Fig. 7. The early post-SAT period was characterized by multiple distinct plumes ranging up to the mid-July maximum of 17 km in altitude. Over longer time periods, vertical mixing produced fewer and more homogeneous layers (a process that one might characterize as the entropification of the originally highly structured plumes). The daily profiles of Fig. S3 of the auxiliary material nicely illustrate this evolution for AHSRL profiles acquired between July 4 and

Aug. 19. After the mid-July peak, the average rate of descent of the maximum backscatter height was relatively rapid ~ 150 m / day) while the upper (and lower) envelopes of the plumes descended at about 15 m / day (at a rate that appears to be tied to the height of the tropopause). Similar AHSRL calculations for the 2008 Kasatochi plume at Eureka yielded a descent rate of ~ 50 m / day.

4.3. Sulphate particle size and refractive index

4.3.1. AERONET retrievals

AERONET inversion retrievals of τ_f, $r_{eff,f}$, σ_f and the real part of the refractive index (m_r) as a function of time for the Eureka ØPAL site are shown in Fig. 8. There is a clear decrease in m_r from a pre-SAT average of 1.45 to a post-SAT average of 1.41 and a net increase in $r_{eff,f}$ from a pre-SAT average of 0.183 to a post-SAT average of 0.250 μm. The pre and post-SAT averages of σ_f remain approximately fixed at 1.58. The post-SAT averages were employed to define the nominal values of the stratospheric sulphate properties in Table 1 with a moderate adjustment to the value of m_r. For the small AODs characteristic of Eureka [AOD(440 nm) < 0.2] the nominal accuracy of m_r and m_i are ±0.05 and 80-100% respectively (*Dubovik et al*., 2000): this latitude of uncertainty, the fact that the ground-based retrievals were confounded by tropospheric contributions and the apriori knowledge at our disposal (that we were looking at plumes of Sarychev sulphates) led to the conclusion that we could permit ourselves the license of fixing m_r and m_i to the values of 1.46 and 0.0 as given by *Russell et al*. (1996) for H_2SO_4-H_20 mixtures (see more details in Table 1).

Results from other high-Arctic sites supported the decision of conserving the ØPAL $r_{eff,f}$ value while modifying the refractive index to more closely match values from the

literature. Fig. 9 shows post-SAT averages for ØPAL, the PEARL ridge laboratory, Thule and Hornsund. All four sites showed consistent results with an increase in τ_f and $r_{eff,f}$. Except for Hornsund the $r_{eff,f}$ and σ_f values are close to the 0.25 μm and 1.6 values found for ØPAL (however we gave considerably less weight to Hornsund results because the number of post-SAT inversions at this site was less than the other sites by a factor of 5 or more). While one can observe a degree of anti-correlation between retrieved values of $r_{eff,f}$ and m_r in the plots of Fig. 8 and Fig. 9, a post-SAT regression between these two variables at ØPAL showed only a marginal anti-correlation ($R^2 = 0.18$) with a (regression driven) decrease in $r_{eff,f}$ of 0.01 μm in changing m_r from a value of 1.41 to 1.46. The authors could not find an explicit estimate of the expected error in $r_{eff,f}$ but the error analysis of *Dubovik et al*. (2000) (including the fact that retrieved PSDs seem to conserve the form of the true PSD in spite of comparatively large retrieval errors in the amplitude of dV / dln r) would suggest that the maximum error ~ $\Delta\tau / \tau_a$ where $\Delta\tau$ is the spectrally averaged optical depth error. For an assumed error of $\Delta\tau \sim 0.02$, a crude average estimate of the maximum $r_{eff,f}$ error for pre and post-SAT conditions would be 33% and 20% respectively.

Results of the SDA / FMC AOD retrieval indicated a similar increase in $r_{eff,f}$ from pre to post-SAT periods but with differences as large as 0.06 and 0.05 μm between the pre-SAT values and between the post-SAT values respectively (there is comparatively little validation of this $r_{eff,f}$ retrieval method compared to AERONET inversions, and no validation in the presence of small Arctic optical depths: we only seek here to point out that a similar trend was observed for a significantly different retrieval method).

These sunphotometry estimates of $r_{eff,f}$ are of course columnar. If one divides the atmosphere into regions above ("+") and below ("-") the tropopause then a plausible weighting scheme can be written as

$$r_{eff,f} = \frac{r_{eff,f}^{(+)} \tau_f^{(+)} + r_{eff,f}^{(-)} \tau_f^{(-)}}{\tau_f} = \gamma\, r_{eff,f}^{(+)} \tau_f^{(+)} + (1 - \gamma)\, r_{eff,f}^{(-)}$$

$$r_{eff,f}^{(+)} = \frac{1}{\gamma}\left(r_{eff,f} - (1 - \gamma)\, r_{eff,f}^{(-)}\right) \qquad (4)$$

where the lack of a superscript implies columnar quantities, $\gamma = \tau_f^{(+)} / \tau_f$ and $\tau_f = \tau_f^{(+)} + \tau_f^{(-)}$. From the AHSRL profiles over Eureka (for cases that were cloud free in the troposphere) we estimated a post-SAT average of 0.6 $\pm$ 0.17 for γ. Assuming that $r_{eff}^{(-)} \sim r_{eff}$(pre-SAT) we obtain a value of $r_{eff}^{(+)} = 0.29$ μm as a post-SAT average (0.27 to 0.34 μm for $\gamma = 0.6 + 0.17$ and $0.6 - 0.17$ respectively).

4.3.2. Retrievals from KARL data at Ny-Ålesund

KARL retrievals performed at Ny-Ålesund supported the contention that Sarychev stratospheric aerosols were generally larger than pre-Sarychev stratospheric aerosols. Fig. 10(a) illustrates retrieval results that were chosen to demonstrate retrieval variability while Fig. 10(b) is a temporal plot of Ny-Ålesund $r_{eff,f}$ retrievals superimposed on the ØPAL retrievals of Fig. 8. The five post-SAT, Ny-Ålesund points represent $r_{eff,f}$ averages of two or more significant stratospheric plumes found in the KARL data on any given day. The error bars correspond to estimated retrieval errors of ± 0.05 μm. The apparent decrease after day 213 (Aug. 1) is not readily apparent in the AERONET retrievals but can't be excluded by any statistical argument between the dates of the 3 KARL points

(Aug. 1 to Sept. 3). The post-SAT retrieval average for the 5 Ny-Ålesund points [using the nomenclature of equation (4)] was $r_{eff,f}^{(+)} = 0.27$ μm.

The retrieved submicron PSDs were both bi-modal and uni-modal as illustrated in Fig. 10(a). With a few minor exceptions, the AERONET submicron PSDs at the four Arctic stations were essentially all uni-modal during the time period of the five KARL post-SAT retrievals. While one can question the inversion stability of bi-modal retrieval features in the presence of an input measurement vector with moderately more information content than a 3-wavelength extinction coefficient spectrum [see *Twomey and Howell* (1967) for example], $r_{eff,f}$ is a robust parameter whose retrieval is commensurate with the information content of the KARL measurements.

4.3.3. Comparisons of retrieved $r_{eff,f}$ with the literature

Our $r_{eff,f}$ results are significantly different from those reported by *Haywood et al*. (2010) who effectively used a value of $r_{eff,f} = 0.13$ μm to model Sarychev sulphates over regional domains that extended up to 80° N (with a log-normal σ_f of 1.4). *Kravitz et al*. (2011) also modeled sulphate particles that were about the size of Haywood's particles in their simulation of Sarychev effects (in actual fact they reverted to small particles of size close to Haywood's after performing initial runs for particle sizes that were near the particle sizes we found in the present work). *Haywood et al*. (2010) further argued that the $r_{eff,f}$ value of 0.25 μm assumed by *Kravitz et al*. (2010) for Kasatochi sulphates was an overestimate. They suggested that an $r_{eff,f}$ of around half that value was a more realistic estimate for "fresh" Sarychev and Kasatochi sulphates and point out that if *Kravitz et al*. (2010) had used that value they would have had better SOD modeling agreement with OSIRIS (the transformation from 550 nm to 750 nm of the modeled

extinction would have produced smaller 750 nm SOD values for smaller particles and thus would have reduced or eliminated model overestimates relative to OSIRIS). While these arguments are sound as far as they go, they do not benefit from the direct (and largely independent) retrievals obtained for the two CIMELs at Eureka, the CIMEL at Thule and the Raman lidar at Ny-Ålesund. It must be said however, that a legitimate counter argument to this last point would be that there were no independent in-situ (airborne) measurement to confirm our claim of larger Sarychev particles. To this we might add that, while there are sound physical reasons for the variable degrees of positive correlation observed between $r_{eff,f}$ and τ_f (see Fig. 8 and 9 for example), one should necessarily be suspicious of retrieval products that covary.

Generic (non Arctic) values of the background stratospheric aerosol are fairly consistent with $r_{eff,f}$ values ~ 0.18 μm (*Russell et al*., 1981, 1996; *Hamill et al*., 1997). With respect to $r_{eff,f}$ variation in the aftermath of an eruption, various authors refer to two or more post-eruption stratospheric modes: one or more lower stratospheric modes of long-duration with an $r_{eff,f}$ varying from near-background values to ~ 0.5 μm) and a second near-tropopause mode of shorter duration with $r_{eff,f}$ values ~ 0.5 – 1.0 μm (*Pueschel et al*., 1994; *Russell et al*., 1996; *Sioris et al*., 2010). These authors associate the former mode with sulphate particles and the latter mode with settled-out ash particles (or ash particles coated with sulphuric acid). A noteworthy, non-Arctic, volcanic-aerosol climatology was produced by *Stothers* (2001) who employed ground-based, spectral extinction measurements to estimate stratospheric $r_{eff,f}$ for the seven largest, aerosol-producing volcanic eruptions in the twentieth century. The results showed a remarkably consistent value of $r_{eff,f}$ ~ 0.3 μm in the first few months after the eruptions.

In terms of Arctic measurements *Pueschel et al*. (1992) defined a background Polar stratospheric aerosol with an $r_{eff,f}$ value of 0.18 μm (and log-normal fit parameters that were quite close to the generic background values noted above). *Hoffman et al*. (2010) estimated a near-tropopause $r_{eff,f}$ value ~ 0.18 μm for a Kasatochi plume at Ny-Ålesund (on Sept. 1, 2008, about 3 weeks after the eruption). *Sioris* (personal communication, 2011) used NIR solar occultation measurements acquired by the MAESTRO spectrometer to retrieve Kasatochi $r_{eff,f}$ averages of 0.35 and 0.3 μm for their lower stratospheric and near-tropopause cases respectively (during the months of October and September respectively). A large $r_{eff,f}$ value of 0.6 μm between these two layers and correspoinding to relatively weak extinction coefficient (*Sioris et al*., 2010) were ascribed to descending ash particles. Their nominal averaging over the northern hemisphere is actually strongly weighted towards the Arctic (because MAESTRO occulation sampling density is considerably greater in the Arctic: c.f. their Fig. 3).

5. Summary and Conclusions

Aerosols from the Sarychev volcano entered the Arctic region less than a week after the strongest SO_2 eruption on June 15 and 16, 2009 and had, by the first week in July, spread out over the entire region. These predominantly stratospheric aerosols were determined to be sub-micron in size and inferred to be composed of sulphates resulting from the condensation of SO_2 gases emitted during the Sarchev eruption.

The average 500 nm Sarychev-induced SODs over Eureka (assumed to be represented by differences between post-SAT and pre SAT averages and labeled ΔSOD) were found to be between 0.03 and 0.05 for τ_f from AERONET inversions and SODs

from AHSRL integrations in the stratosphere. Given the pre-Sarychev, AHSRL average of ~ 0.01 in SOD, this implies that the Sarychev contribution to post-Sarychev SODs was approximately a factor of 3 to 5 larger than pre-Sarychev SODs.

The AHSRL values are about a factor of two higher than OSIRIS estimates: we have argued that OSIRIS FOV averaging effects produce low frequency representations of high frequency extinction profiles but that this alone should not produce a reduction in the average amplitude of extinction coefficients and derived SODs. We also showed that the apparent OSIRIS underestimates of ΔSOD are not related to the choice of sulphate model (the choice of big or small $r_{eff,f}$) since OSIRIS ΔSODs at 750 nm remain significantly less than sunphotometer derived ΔSODs at 750 nm.

The 500 nm sunphotometry and AHSRL ΔSOD values are also significantly larger than the modeling estimates of *Haywood et al*. (2010) for a latitude band around 80° N: their ΔSOD at 500 nm [derived from Fig. 6(d) of their paper while using our sulphate model to transform from 750 to 500 nm] would be ~ 0.01 for the combined months of July and August. ΔSOD averages at Ny-Ålesund for July were within the error (standard deviation) margins of the Eureka sunphotometry and AHSRL results (the AHSRL results were high relative to the sunphotometry and the Ny-Ålesund estimates for August: this may have have resulted from the fact that the AHSRL sampling was sparse and probably unrepresentative during that month).

The Eureka lidar e-folding time measured from a regression start date (t_0) of July 27, 2009 was 4.0 months. Our computations for OSIRIS SODs yielded e-folding times, again referenced to a t_0 of July 27 of 3.0 and 3.9 months respectively for the near-Eureka and Pan-Arctic (70 to 80° N) cases. The near-Eureka value was found to be sensitive to a

rather rapid decay in OSIRIS SODs in the first two weeks in October: the e-folding time calculation was found to increase by ~ month if one or two weeks in October were eliminated from the exponential regression.

CALIOP data were instrumental in helping to demonstrate the nature and spatial dynamics of the Sarychev sulphates. It was nonetheless found that care had to be taken when employing stratospheric CALIOP SODs. The noisy character of daytime backscatter returns induced an artifactual SOD "hole" in pan-Arctic views of CALIOP retrievals and an artifactual minimum in the temporal, pan-Arctic CALIOP SOD response to Sarychev sulphates. A second example of the need for thoughtful employment of CALIOP data involved the lack of a sub-classification for phenomena labeled as stratospheric layers: we did find examples of high depolarization (non fine mode) data being classified as a stratospheric feature and accordingly false positives for fine mode aerosols if no subclassification of the stratospheric layer class was employed. This subclassification into high and low depolarization SODs affected the pre-SAT results but did not significantly affect the post-SAT results (this latter result being coherent with our supposition that Sarychev aerosols were characterized by low depolarization).

Lidar profiles at Eureka acquired immediately after the SAT, indicated the presence of multiple plumes where the maximum backscattering plume was between the tropopause and 17 km altitude. After about two months, the initial complex vertical plume structures had collapsed into fewer, more homogeneous plumes near the tropopause.

Retrievals of $r_{eff,f}$ and σ_f for the two Eureka sites and Thule were remarkably consistent with post-SAT averages being close to 0.25 μm and 1.6 respectively. The

stratospheric analogue to the columnar $r_{eff,f}$ average was estimated to be $r_{eff,f}^{(+)} = 0.29$ μm for Eureka data. Raman lidar retrievals at Ny-Ålesund yielded a post-SAT average of $r_{eff,f}^{(+)} = 0.27$ μm. These values are about 50% larger than background stratospheric values. They also exceed, by more than a factor of two, the values chosen by *Haywood et al*. (2010) and *Kravitz et al*. (2011) for their global modeling of Sarychev sulphates.

Such differences in particle size have non trivial consequences on radiative forcing and climate engineering arguments: an approximate doubling of effective particle size from Haywood's $r_{eff,f}$ of 0.13 μm to the value of 0.25 μm in Table 1 (and using the refractive index of Table 1) results in a 5 fold increase in the hemispherical (per particle) backscattering cross section of sulphate particles (the result of a 30% decrease in hemispherical backscatter fraction accompanied by an 8 fold increase in scattering cross section: the 8 fold increase results from the product of a near 3 fold increase in average, per particle, scattering area and a near 3 fold increase in optical scattering efficiency).

Symbol and acronym glossary

AEROCAN	Canadian network of CIMEL sunphotometers / sky radiometers. AEROCAN is a subnetork of AERONET.
AERONET	NASA-led global network of CIMEL sunphotometers / sky radiometers
AOD	Aerosol Optical Depth [unitless]
β_a	Aerosol backscattering coefficient (also known as the aerosol backscatter

	cross section) [km^{-1} sr^{-1}]
δ_a	Aerosol depolarization ratio [unitless]
ΔSOD	Estimate of the SOD due to Sarychev sulphates
MAESTRO	Measurement of Aerosol Extinction in the Stratosphere and Troposphere. This an occultation spectrometer on the SCISAT satellite.
OD	Optical Depth [unitless]
ØPAL	Sea-level CIMEL site at Eureka (10 m. elevation)
OSIRIS	Optical Spectrograph and InfRared Imaging System
PEARL	Polar Environmental Atmospheric Research Laboratory. It was also the original name for the Ridge laboratory at 610 m. elevation
post-SAT, pre-SAT	see SAT below
PSD	Particle Size Distribution
$r_{eff, f}$	Effective radius of the fine mode distribution in μm (see Table 1)
σ_f	Logarithmic standard deviation (see Table 1)
S_a	lidar ratio (also known as the extinction to backscatter ratio) [sr]

SAT, pre-SAT, post-SAT	Sarychev Arrival Time – date when Sarychev plume effects are detected at a given measuring site. Unless otherwise indicated "pre-SAT" refers to a period from May 1, 2009 to the SAT and post-SAT refers to the combination of July and August, 2009
SOD	Stratospheric Optical Depth: particulate optical depth above the thermal tropopause (above the 380 °K level in the unique case of the OSIRIS data that was averaged over the 70° to 80° N latitude band)

Acknowledgements

The authors would like to thank four Canadian funding agencies, NSERC (National Sciences and Engineering Research Council), CFCAS (Canadian Foundation for Climate and Atmospheric Sciences), CFI (Canadian Foundation for Innovation) and FQRNT (Fonds de recherche sur la nature et les technologies, Québec) for their financial support. Valuable support was also provided by Environment Canada and NASA's AERONET, CALIPSO and MODIS projects. We thank the PIs of Thule, Greenland and Hornsund, Spitsbergen (Brent Holben and Piotr Sobolewski) for the use of their AERONET data. The contributions of Matthew Okraszewski, Alexei Khmel, and Oleg Mikhailov of the CANDAC ops team are also gratefully acknowledged.

References

Anon (2006), AERONET Inversion Products, AERONET document available from the AERONET web site.

Bluth, G. J. S., W. I. Rose, I. E. Sprod, and A. J. Krueger (1997), Stratospheric loading of sulfur from explosive volcanic eruptions, *J. Geol.*, 105(6), 671-683.

Bourdages, L., T. J. Duck, G. Lesins, J. R. Drummond, and E. Eloranta (2009), Physical properties of High Arctic tropospheric particles during winter, *Atmos. Chem. Phys.*, 9, 6881 - 6897.

Bourassa, A. E., D. A. Degenstein, R. L. Gattinger, and E. J. Llewellyn (2007), Stratospheric aerosol retrieval with optical spectrograph and infrared imaging system limb scatter measurements, *J. Geophys. Res.*, 112, D10217, doi:10.1029/2006JD008079.

Bourassa, A. E., D. A. Degenstein, B. J. Elash, and E. J. Llewellyn (2010), Evolution of the stratospheric aerosol enhancement following the eruptions of Okmok and Kasatochi: Odin-OSIRIS measurements, *J. Geophys. Res.*, 115, D00L03, doi:10.1029/2009JD013274.

Caldeira, K., and L. Wood (2008), Global and Arctic climate engineering: Numerical model studies, *Philos. Trans. Royal Soc. A*, 366(1882), 4039-4056, doi:10.1098/rsta.2008.0132.

Dubovik, O. and M. D. King (2000), A flexible inversion algorithm for retrieval of aerosol optical properties from Sun and sky radiance measurements, *J. Geophys. Res.*, 105, 20 673-20 696.

Dubovik, O., A. Smirnov, B. N. Holben, M. D. King, Y.J. Kaufman, T. F. Eck, and I. Slutsker (2000), Accuracy assessments of aerosol optical properties retrieved from AERONET sun and sky-radiance measurements, *J. Geophys. Res.*, 105, 9791-9806.

Eloranta, E. W. (2005), High Spectral Resolution Lidar in Lidar: Range-resolved optical remote sensing of the atmosphere, K. Weitkamp (editor), Springer Series in Optical Sciences, Springer-Verlag, New York.

Eloranta, E. W., I. A. Razenkov, J. P. Garcia, and J. Hedrick (2006), Observations with the University of Wisconsin Arctic High Spectral Resolution Lidar, ILRC22, July 12-16, Matera, Italy.

Hamill, R., E. J. Jensen, P. B. Russell, and J. J. Bauman, The life cycle of stratospheric aerosol particles, *Bull. Amer. Meteorol. Soc*., 78(7), 1395-1410, 1997.

Hansen, J. E., and L. D. Travis (1974), Light scattering in planetary atmospheres, *Space Science Reviews*, 16, 527-610.

Haywood, J. M., A. Jones, L. Clarisse, A. Bourassa, J. Barnes, P. Telford, N. Bellouin, O. Boucher, P. Agnew, C. Clerbaux, P. Coheur, D. Degenstein, and P. Braesicke (2010), Observations of the eruption of the Sarychev volcano and simulations using the HadGEM2 climate model, *J. Geopys. Res*., 115, D21212, doi:10.1029/ 2010JD014447.

Hoffman, A., C. Ritter, M. Stock, M. Maturilli, S. Eckhardt, A. Herber, and R. Neuber (2010), Lidar measurements of the Kasatochi aerosol plume in August and September 2008 in Ny-Ålesund, Spitsbergen, *J. Geophys. Res.*, 115, doi:10.1029/2009JD013039.

Kravitz, B., and A. Robock (2011), Climate effects of high latitude volcanic eruptions: Role of the time of year, *J. Geopys. Res.*, *116*, D01105, doi:10.1029/2010J D014448.

Kravitz, B., A. Robock, and A. Bourassa (2010), Negligible climatic effects from the 2008 Okmok and Kasatochi volcanic eruptions, *J. Geophys. Res.*, 115, D00L05, doi:10.1029/2009JD013525.

Kravitz, B., A. Robock, A. Bourassa, T. Deshler, D. Wu, I. Mattis, F. Finger, A. Hoffmann, C. Ritter, L. Bitar, T. Duck, and J. Barnes (2011), Simulation and observations of stratospheric aerosols from the 2009 Sarychev volcanic eruption, *J. Geophys. Res.*, doi:10.1029/2010JD015501, in press.

Krotkov, N. A., S. A. Carn, A. J. Krueger, P. K. Bhartia, and K. Yang (2006), Band Residual Difference Algorithm for Retrieval of SO_2 From the Aura Ozone Monitoring Instrument (OMI), *IEEE Trans. Geos. Rem. Sens.*, 44(5), 1259-1266.

Liu, Z., M. A. Vaughan, D. M. Winker, C. Kittaka, R. E. Kuehn, B. J. Getzewich, C. R. Trepte, and C. A. Hostetler (2009), The CALIPSO lidar Cloud and Aerosol Discrimination: Version 2 Algorithm and Initial Assessment of Performance, *J. Atmos. Ocean. Technol.*, 26, 1198-1213, doi:10.1175/2009JTECHA1229.1.

Lam, K. S., V. Savastiouk, W. Y. Fung, T. K. Chan, and K. Lamb (2007), Recalculation of 11-year total ozone of Brewer spectrophotometer 115, *J. Geophys. Res.*, 112, D15104, doi:10.1029/2006JD008178.

Nott, G. J. , T. J. Duck, J. G. Doyle, M. E. W. Coffin, C. Perro, C. P. Thackray, J. R. Drummond, P. F. Fogal, E. McCullough, and R. J. Sica (2011), A remotely-operated lidar for aerosol, temperature, and water vapor profiling in the High Arctic, *J. Atmos. Oceanic Tech.*, doi:10.1175/JTECH-D-11-00046.1, in press.

O'Neill, N. T., T. F. Eck, A. Smirnov, B. N. Holben, and S. Thulasiraman (2003), Spectral discrimination of coarse and fine mode optical depth, *J. Geophys. Res.*, 108(15), 4559, doi:10.1029/2002jd002975.

O'Neill, N. T., S. Thulasiraman, T. F. Eck, and J. S. Reid (2008a), Correction to the effective radius expression in O'Neill et al. (2005), *J. Geophys. Res.*, 113, D24203, doi:10.1029/2008JD011334.

O'Neill, N. T., O. Pancrati, K. Baibakov, E. Eloranta, R. L. Batchelor, J. Freemantle, L. J. B. McArthur, K. Strong, and R. Lindenmaier (2008b), Occurrence of weak, sub-micron, tropospheric aerosol events at high Arctic latitudes, *Geophys. Res. Lett.*, 35, L14814, doi:10.1029/2008GL033733.

Pueschel, R. F., G. V. Ferry, K. G. Snetsinger, J. Goodman, J. E. Dye, D. Baumgardner, and B. W. Gandrud (1992), A Case of Type I Polar Stratospheric Cloud Formation by Heterogeneous Nucleation, *J. Geophys. Res.*, 97(D8), 8105-8114.

Pueschel, R., P. Russell, D. Allen, G. Ferry, K. Snetsinger, J. Livingston, and S. Verma (1994), Physical and optical properties of the Pinatubo volcanic aerosol: Aircraft observations with impactors and a Sun-tracking photometer, *J. Geophys. Res.*, 99(D6), 12915-12922.

Robock, A. (2000), Volcanic eruptions and climate, *Rev. Geophys.*, 38(2), 191-219, doi: doi:10.1029/1998RG000054.

Russell, P. B., J. M. Livingston, T. J. Swissler, M. P. McCormick, W. P. Chu, T. J. Pepin (1981), Satellite and Correlative Measurements of the Stratospheric Aerosol. I: An Optical Model for Data Conversions, *J. Atmos. Sci.*, 38, 1279–1294.

Russell, P. B., J. M. Livingston, R. F. Puesche1, J. J. Bauman , J. B. Pollack, S. L. Brooks, P. Hamill, L. W. Thomason, L. L. Stowe, T. Deshler, E. G. Dutton, and W. Bergstrom (1996), Global to microscale evolution of the Pinatubo volcanic aerosol

derived from diverse measurements and analyses, *J. Geophys. Res.*, 101(D13), 18745-18763.

Saha, A., N. T. O'Neill, E. Eloranta, R. S. Stone, T. F. Eck, S. Zidane, D. Daou, A. Lupu, G. Lesins, M. Shiobara, and L. J. B. McArthur (2010), Pan-Arctic sunphotometry during the ARCTAS-A campaign of April 2008, *Geophys. Res. Lett.*, 37, L05803, doi:10.1029/2009GL041375.

Savastiouk, V., and C. T. McElroy (2005), Brewer spectrophotometer total ozone measurements made during the 1998 middle atmosphere nitrogen trend, *Atmos. Ocean*, 43, 315-324.

Sioris, C. E., C. D. Boone, P. F. Bernath, J. Zou, C. T. McElroy, and C. A. McLinden (2010), Atmospheric Chemistry Experiment (ACE) observations of aerosol in the upper troposphere and lower stratosphere from the Kasatochi volcanic eruption, *J. Geophys. Res.*, 115, D00L14, doi:10.1029/2009JD013469.

Sroga, J. T., E. W. Eloranta, S. T. Shipley, F. L. Roesler and P. J. Tryon (1983), High spectral resolution lidar to measure optical scattering properties of atmospheric aerosols. 2: Calibration and data analysis, *App. Opt.*, 22(23), 3725-3732.

Stothers, R. B. (2001), A chronology of annual mean effective radii of stratospheric aerosols from volcanic eruptions during the twentieth century as derived from ground-based spectral extinction measurements, *J. Geophys. Res.*, 106, 32,043–32,049, doi:10.1029/2001JD000414.

Twomey, S., and H. B. Howell (1967), Some aspects of the optical estimation of microstructure in fog an cloud, *App. Opt.*, 6(12), 2125-2131.

Vaughan, M. A., D. M. Winker, and K. A. Powell (2005), CALIOP ATBD – Part 2: Feature detection and layer properties algorithms, PC-SCI-202 Part 2, Release 1.01, Sept. 27, 2005.

Weitkamp, C. (2005), Lidar: Range resolved optical remote sensing of the atmosphere, Springer Series in Optical Sciences, Springer-Verlag, New York.

Winker, D. M., W. H. Hunt, and M. J. McGill (2007), Initial performance assessment of CALIOP, *Geophys. Res. Lett.*, 34, L19803, doi:10.1029/2007GL030135.

Fig. 1: Variation of stratospheric aerosols and SO_2 at Eureka on July 1 and 2, 2009: (a) and (b) backscatter cross section and depolarization ratio of the AHSRL (c) total, fine and coarse mode aerosol optical depth at 500 nm using the SDA algorithm applied to AERONET Level 1.0 (high frequency) data, the grey points represent stratospheric optical depths obtained by integrating the AHSRL backscatter coefficient profiles from the tropopause (purple curve) to about 14 km altitude (d) fine mode optical depth and SO_2 columnar concentration. The maximum sampling frequency of the Level 1.0 AERONET data is substantially less than once every 3 minutes: indeed 2009 data at ØPAL turned to have an anomalously low sampling rate compared to other years (median sampling rate of once every 15 minutes versus once every 3 minutes in other years).

Fig. 2: Comparison of CALIOP SODs and OMI SO_2 columnar concentrations on July 1 and 2, 2009. The CALIOP images were obtained using "non-zero" SOD values averaged over lat. / long. grid cells of 2° x 10°. The non-zero SOD values are associated with stratospheric layers and represent standard CALIOP products.

Fig. 3: Estimated 500 nm, daily averaged, SODs at Eureka before and after the arrival of the Sarychev plume. The CRL and AHSRL SODs were obtained from backscatter coefficient integrations carried out above the tropopause curve of Fig. 5 and using the 532 nm lidar ratio of Table 1. All SODs were re-processed to the common wavelength of 500 nm using the parameters of Table 1. Sunphotometer optical depths are estimates of total columnar fine-mode optical depth (τ_f) from the SDA/FMC algorithm. OSIRIS SODs are derived from single profiles (they are not daily averages).

Fig. 4: 5-day averages of CALIOP SOD (532 nm) from a few weeks before the SAT (Sarychev Arrival Time) to the last week in September. The SODs employed for this image mosaic were non-zero SODs of the stratospheric layer class.

Fig. 5: (a) Number of CALIOP samples employed in computing pan-Arctic SODs for the 10 day averages of Fig. 5(b). Pan-Arctic refers to the area north of the Arctic Circle. The black segmented line corresponds to all CALIOP samples classified as stratospheric layers, the red segmented line corresponds to the subset of these samples with $\delta_a \leq 0.2$ and the blue segmented line corresponds to the subset of the samples with $\delta_a > 0.2$.

(b) estimated, Pan-Arctic, CALIOP SOD and OMI-SO_2 columnar concentration. The high frequency (circular symbol) plots are one day averages. The broken vertical line represents the SAT for the whole Arctic (determined to be June 19, 2009). The lidar ratio of Table 1 (59 sr) was used for the low δ_a cases, 25 sr for the high δ_a cases and a sample-weighted mean for the mixed (black segmented line). The low-δ_a SOD curves were filtered to eliminate small-sample cases [see Text S1 of the auxiliary material (Section 1)]. The general processing and averaging logistics are described in the caption of Fig. 2.

(c) CALIOP plot of (b) along with an equivalent 10-day averaging scheme applied to OSIRIS data that was first averaged over the latitude region between 70° and 80° N.

Fig. 6: Summary OD statistics at 500 nm for the pre-SAT and post-SAT periods and the difference between these two periods. Fig. 6(a) shows these averages applied to Eureka data (the temporal profiles of Fig. 3), where the pre-SAT averages were taken from May 1 (DOY = 121) to the end of June 24, 2009 (DOY = 175) except for the CRL whose average was taken over the available points from Feb. to May. Fig. 6(b) shows

pan-Arctic results for CALIOP and OSIRIS SOD averages north of the Arctic circle and between 70° and 80° N respectively (the SAT date in this case was taken as June 19, 2009). The error bars represent standard deviations (in the case of ΔSOD, the error bars were taken to be the square root of the quadratic sum of the individual standard deviations). Details on the different retrievals are given in Table 2.

Fig. 7: Variation of stratospheric plume heights over Eureka as deduced from the AHSRL and CRL lidars. The circular symbols represent the altitude of maximum β_a while the green line represents the tropopause height as deduced from Environment Canada radiosonde data. The grey area represents the range of heights associated with multiple plumes (or the thickness of what appeared to be fewer thicker plumes, months after the beginning of the Sarychev intrusion over Eureka).

Fig. 8: Temporal variation of key AERONET inversion parameters at Eureka: from top to bottom, τ_f, $r_{eff,f}$, σ_f and the real part of the refractive index (m_r). The color scheme is significant; while red is reserved for fine mode particles throughout this work, the AERONET retrievals of refractive index are carried out independently of particle size (at least explicitly, implicitly, greater numbers of particles in a given size mode will have a greater influence on the retrieved refractive index).

Fig. 9: Pre and post SAT τ_f, $r_{eff,f}$, σ_f and m_r values from the AERONET inversion for 4 AEROCAN / AERONET high-Arctic stations. The pre and post SAT periods were from approximately the beginning of May to the SAT and from the SAT to the end of August (the SATs were June 25 and June 22 respectively at the ØPAL and PEARL sites of Eureka and the Thule site in Greenland). These results were computed for Level 1.5

AERONET data. The standard deviations for the pre and post SAT periods are shown as error bars.

Fig. 10: (a) Particle size distribution retrievals for Sarychev plumes at Ny-Ålesund. (b) Time series of retrieved $r_{eff,f}$ values at ØPAL (in red) and Ny-Ålesund (in green).

Table 1: Nominal optical and microphysical parameters characterizing stratospheric aerosols at Eureka after the arrival of Sarychev sulphates at that site on or about June 25, 2009 (the SAT or Sarychev Arrival Time). These nominal parameters are largely based on post-SAT averages of AERONET inversion retrieval parameters at the ØPAL site with some moderate disparities. The post-SAT averaging was from the SAT to Aug. 31, 2009.

m_r (real part of the refractive index)[1]	1.46
m_i (real part of the rerfractive index)[2]	0.0
$r_{eff,f}$ (effective radius of the fine mode)[3]	0.25 μm
σ_f (logarithmic standard deviation)[4]	1.6
$r_{N,f}$ (geometric mean for the number density distribution)[5]	0.144 μm
S_a (lidar ratio) at 532 nm [6]	59 sr
Extinction transformation factor: 750 to 500 nm [$C_{ext}(500) / C_{ext}(750)$][6]	1.636
Extinction transformation factor: 532 to 500 nm [$C_{ext}(500) / C_{ext}(532)$][6]	1.058

[1] Assigned value (H_2SO_4-H_20 mixtures) from the tables of *Russel et al*. (1996). Specifically the sub-table for T = -50°C, λ = 500 or 532 nm, H_2SO_4 weight % = 78.6. The average of the AERONET inversion was 1.41 for the post-SAT average.

[2] $m_i < 10^{-6}$ for visible wavelengths (*Russel et al*. (1996). The average of the AERONET inversion was 0.0038 for the post-SAT average.

[3] Post-SAT average of $r_{eff,f}$ from the AERONET inversion (see *Hansen and Travis*, 1974 for the first-principle definition of r_{eff})

[4] Post-SAT average of σ_f from the AERONET inversion. σ_f = exp(*StdDev-F*) where "*StdDev-F*" is the standard deviation in *ln r* space (and is the exact nomenclature used in the AERONET inversion product):

$$StdDev - F = \sqrt{\frac{\int_{r\,min}^{r\,max} (\ln r - \ln r_v)^2 \frac{dV}{d\ln r} d\ln r}{\int_{r\,min}^{r\,max} \frac{dV}{d\ln r} d\ln r}}$$

where r_v is the geometric mean radius for the volume distribution (AERONET inversion product called "VolMedianRad-F"). Note that σ_f is independent of the type of distribution (number, surface or volume density) if the distribution is log-normal.

[5] $r_{N,f} = r_{eff,f} \exp(-2.5 \ln^2 \sigma)$. This analytical, log-normal formulation uses the post-SAT averages of $r_{eff,f}$ and σ_f to compute a log-normal-equivalent value for the geometric radius.

[6] Mie calculations for a log-normal distribution ($r_{N,f}$, σ_f, m_r and m_i given above). C_{ext} represents the extinction cross section (with units of μm^2, for example).

Table 2: Definitions of the Fig. 6 acronyms

AHSRL Eureka	Averages of the daily average SODs described in the caption of Fig. 3.
CRL Eureka	Averages of the daily average SODs described in the caption of Fig. 3.
CALIOP pan-Arctic	Averages of the 10-day averages described in the caption of Fig. 5 (for the case of $\delta_a \leq 0.2$).
OSIRIS Eureka	SODs from OSIRIS limb retrievals of extinction coefficient profiles acquired within 270 km of Eureka. These profiles were integrated from near the tropopause to around 30 km (exact altitudes varied as per the discussion in the instrumentation section).
OSIRIS pan-Arctic	Averages of SODs from OSIRIS limb retrievals of extinction coefficient profiles between 70 and 80° N latitude. Extinction coefficient profiles were integrated from the 380° K potential temperature level to around 30 km.
SunPh Eureka (AERONET inversion)	τ_f average at the Eureka ØPAL site.
SunPh Eureka (SDA Level 2.0)	τ_f average at the Eureka ØPAL site (data of Fig. 3).

Table 3: e-folding time (in months). The reference time [t_0 of equation (3)] is taken as July 27, 2009, roughly one month after the SAT. The exponential regressions were all of the form SOD(t) except for *Haywood et al*. (2010)

Eureka Lidars	OSIRIS (near Eureka)	OSIRIS (80^oN band)	OSIRIS (70^o-80^oN)
4.0[a]	3.0[a]	2.1[b]	3.9[a] 2.7[c]

[a] this study

[b] *Haywood et al*. (2010): e-folding time computed from an exponential regression of $\Delta SOD = a \exp(-bt)$

[c] *Kravitz et al*. (2011)

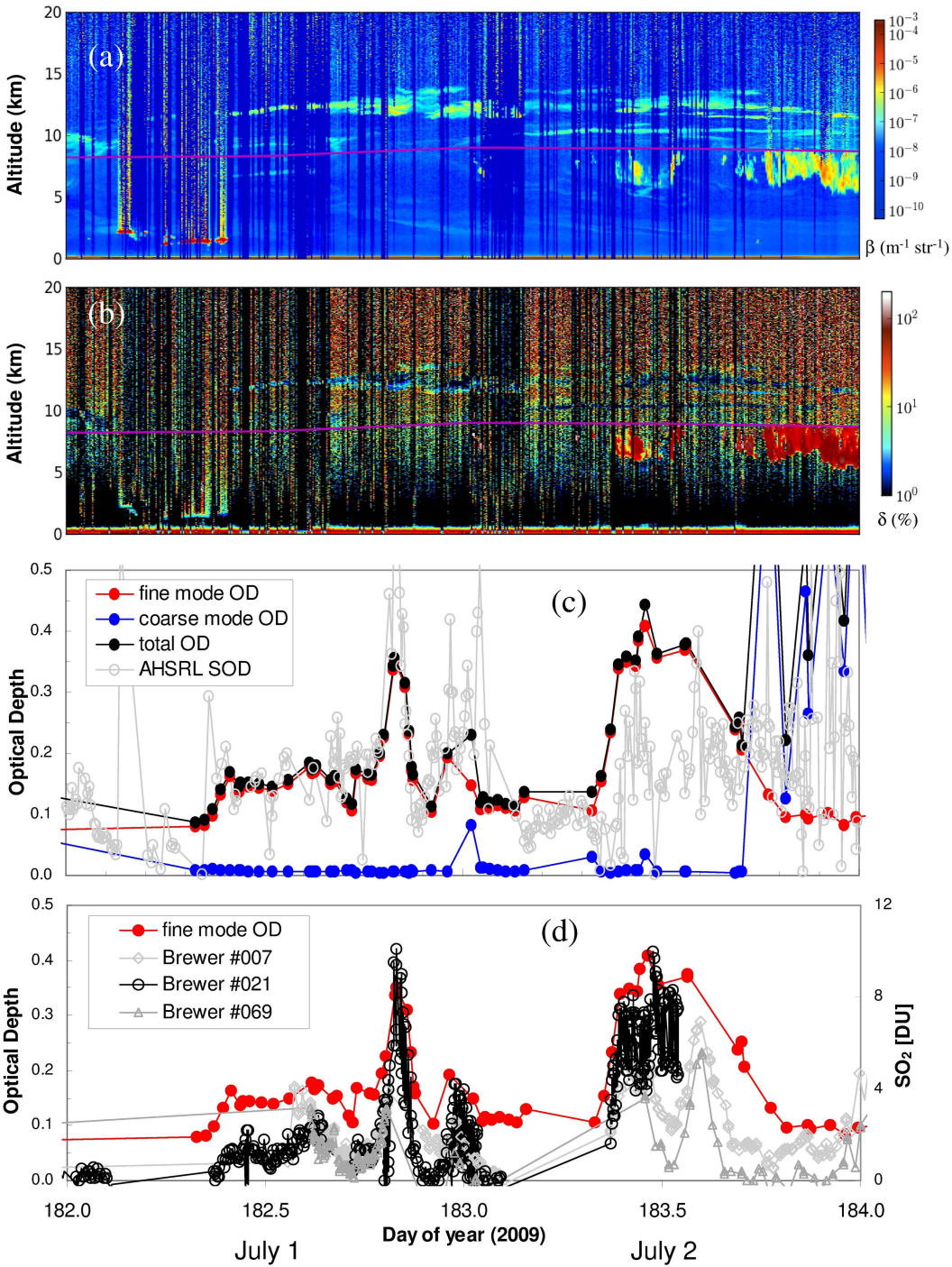
(a)
Altitude (km)
β (m⁻¹ str⁻¹)
(b)
Altitude (km)
δ (%)
(c)
fine mode OD
coarse mode OD
total OD
AHSRL SOD
Optical Depth
(d)
fine mode OD
Brewer #007
Brewer #021
Brewer #069
Optical Depth
SO2 [DU]
Day of year (2009)
July 1
July 2

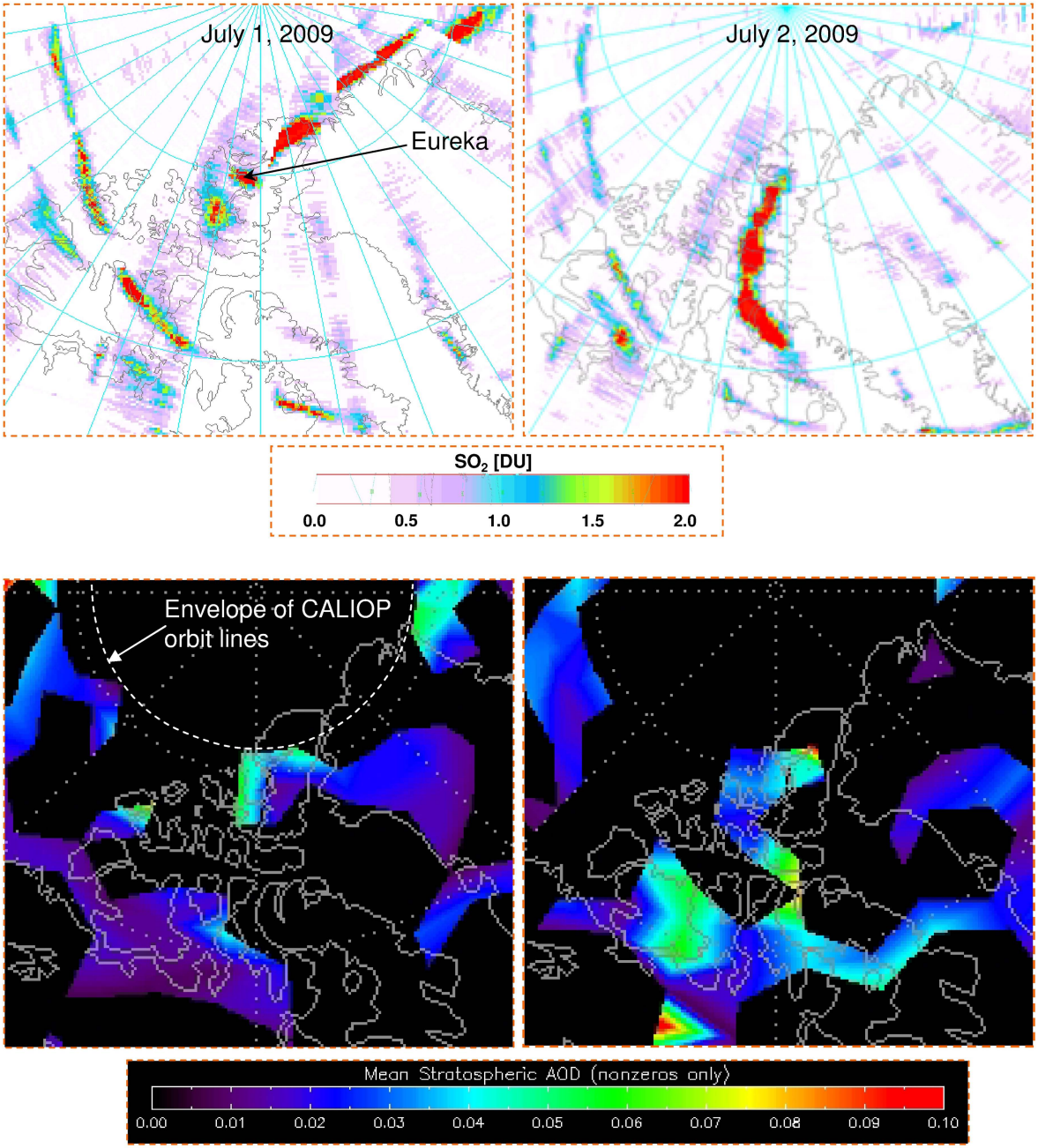
July 1, 2009
Eureka
July 2, 2009
SO2 [DU]
0.0
0.5
1.0
1.5
2.0
Envelope of CALIOP
orbit lines
Mean Stratospheric AOD (nonzeros only)
0.00
0.01
0.02
0.03
0.04
0.05
0.06
0.07
0.08
0.09
0.10

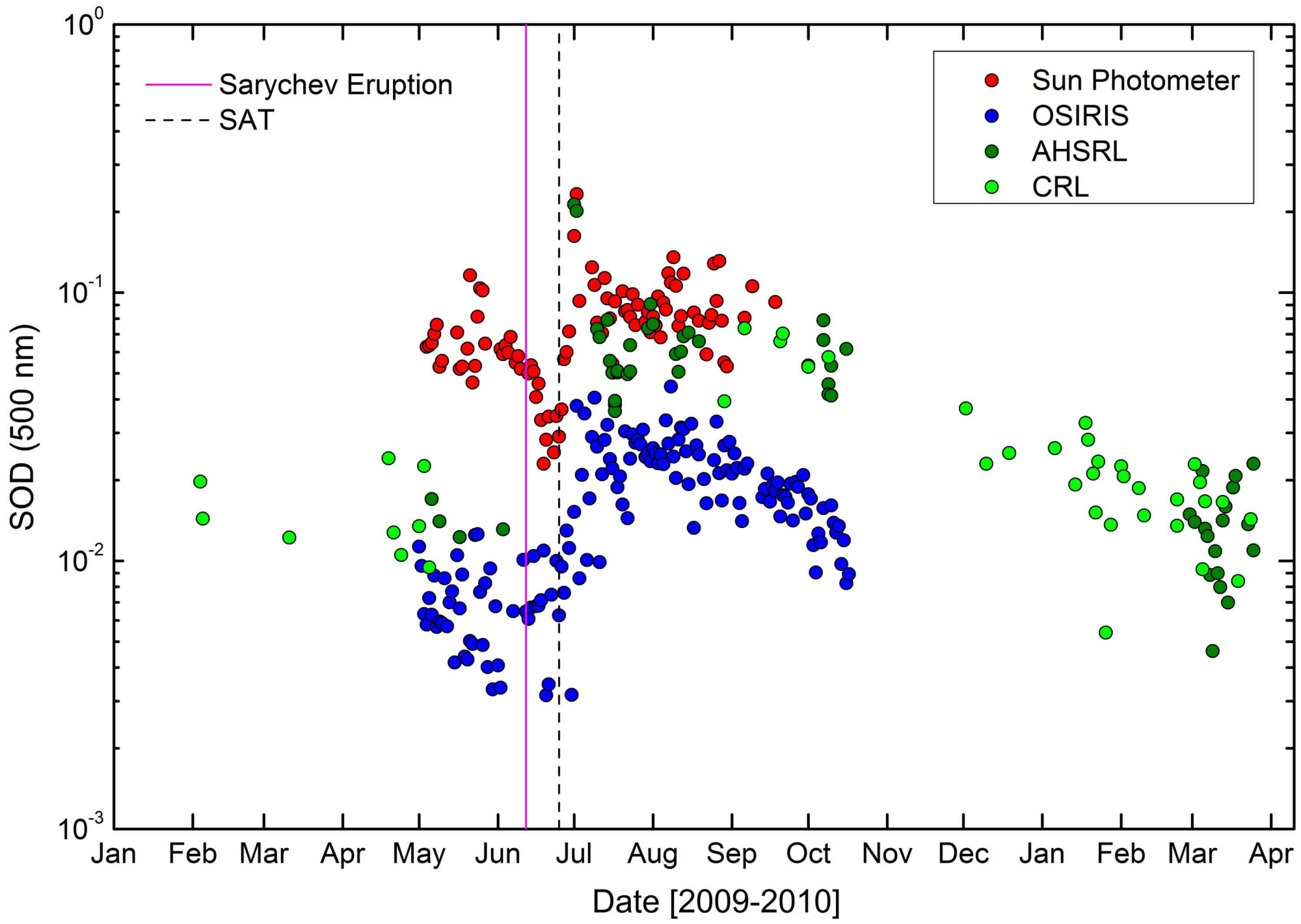
Sarychev Eruption
SAT
Sun Photometer
OSIRIS
AHSRL
CRL
SOD (500 nm)
10^{0}
10^{-1}
10^{-2}
10^{-3}
Jan
Feb
Mar
Apr
May
Jun
Jul
Aug
Sep
Oct
Nov
Dec
Jan
Feb
Mar
Apr
Date [2009-2010]

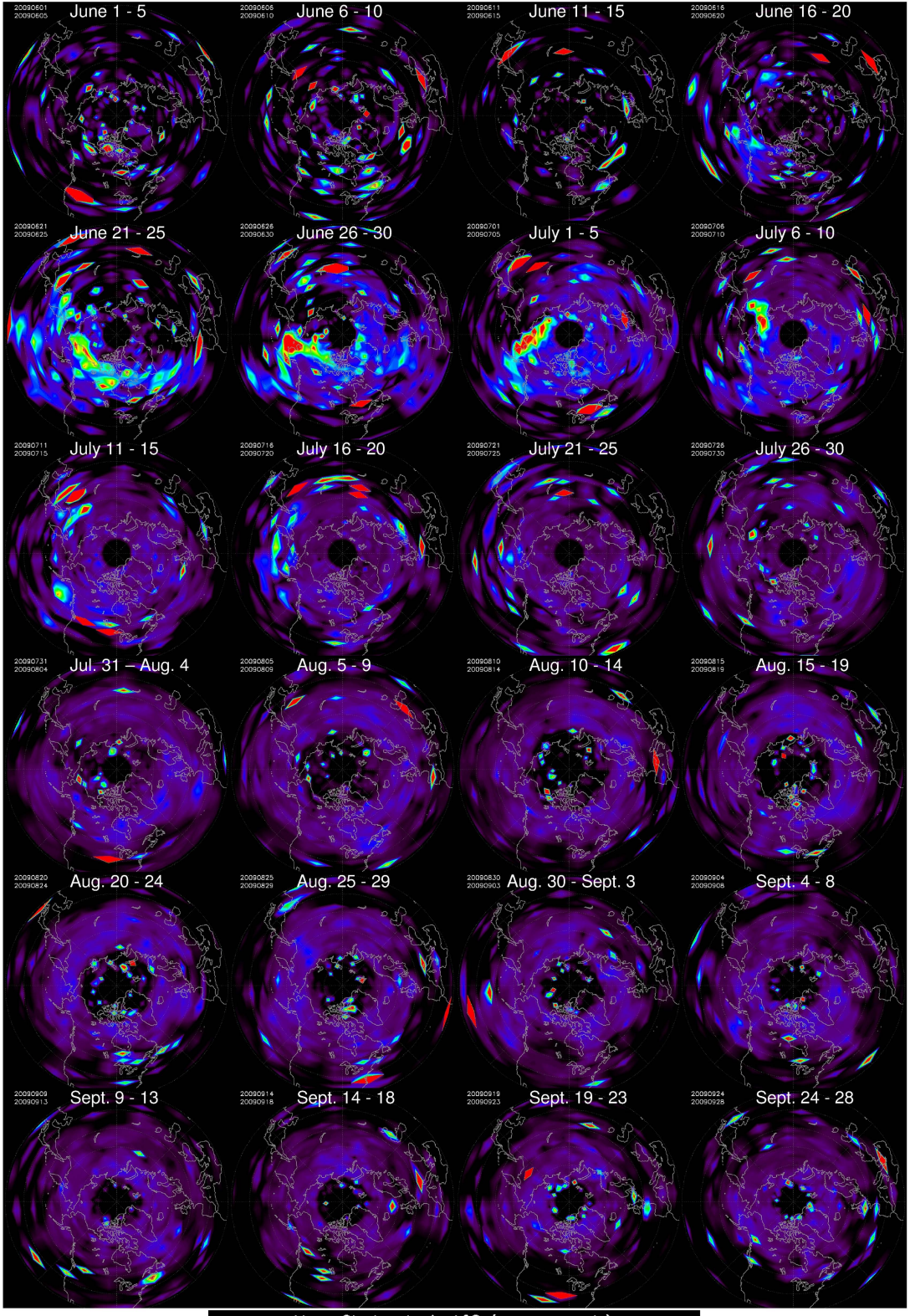
20090601
20090605
June 1 - 5
20090606
20090610
June 6 - 10
20090611
20090615
June 11 - 15
20090616
20090620
June 16 - 20
20090621
20090625
June 21 - 25
20090626
20090630
June 26 - 30
20090701
20090705
July 1 - 5
20090706
20090710
July 6 - 10
20090711
20090715
July 11 - 15
20090716
20090720
July 16 - 20
20090721
20090725
July 21 - 25
20090726
20090730
July 26 - 30
20090731
20090804
Jul. 31 – Aug. 4
20090805
20090809
Aug. 5 - 9
20090810
20090814
Aug. 10 - 14
20090815
20090819
Aug. 15 - 19
20090820
20090824
Aug. 20 - 24
20090825
20090829
Aug. 25 - 29
20090830
20090903
Aug. 30 - Sept. 3
20090904
20090908
Sept. 4 - 8
20090909
20090913
Sept. 9 - 13
20090914
20090918
Sept. 14 - 18
20090919
20090923
Sept. 19 - 23
20090924
20090928
Sept. 24 - 28
Mean Stratospheric AOD (nonzeros only)
0.00 0.01 0.02 0.03 0.04 0.05 0.06 0.07 0.08 0.09 0.10

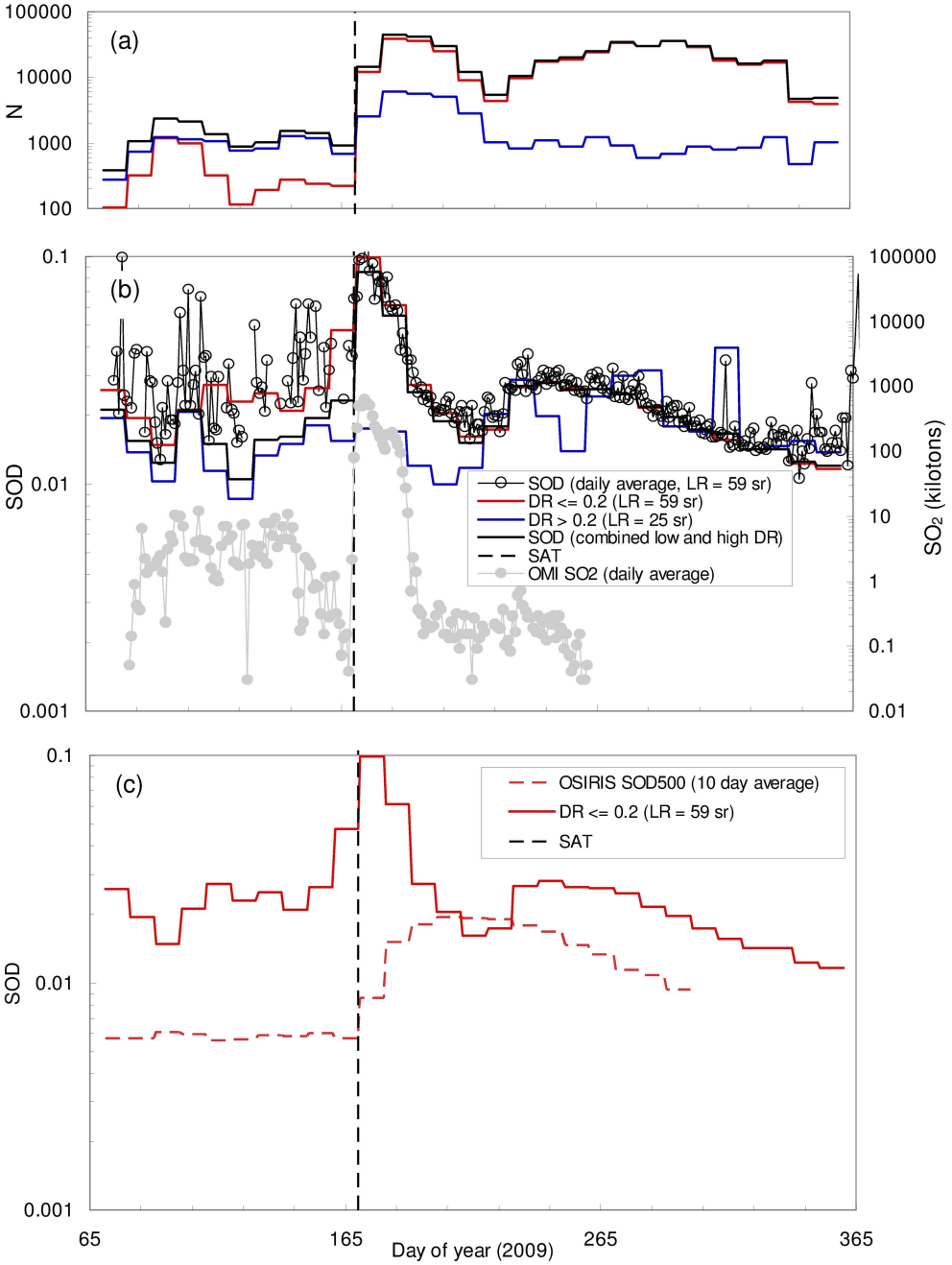
(a)
N
100000
10000
1000
100
(b)
SOD
0.1
0.01
0.001
100000
10000
1000
100
10
1
0.1
0.01
SO2 (kilotons)
SOD (daily average, LR = 59 sr)
DR <= 0.2 (LR = 59 sr)
DR > 0.2 (LR = 25 sr)
SOD (combined low and high DR)
SAT
OMI SO2 (daily average)
(c)
SOD
0.1
0.01
0.001
OSIRIS SOD500 (10 day average)
DR <= 0.2 (LR = 59 sr)
SAT
65
165
265
365
Day of year (2009)

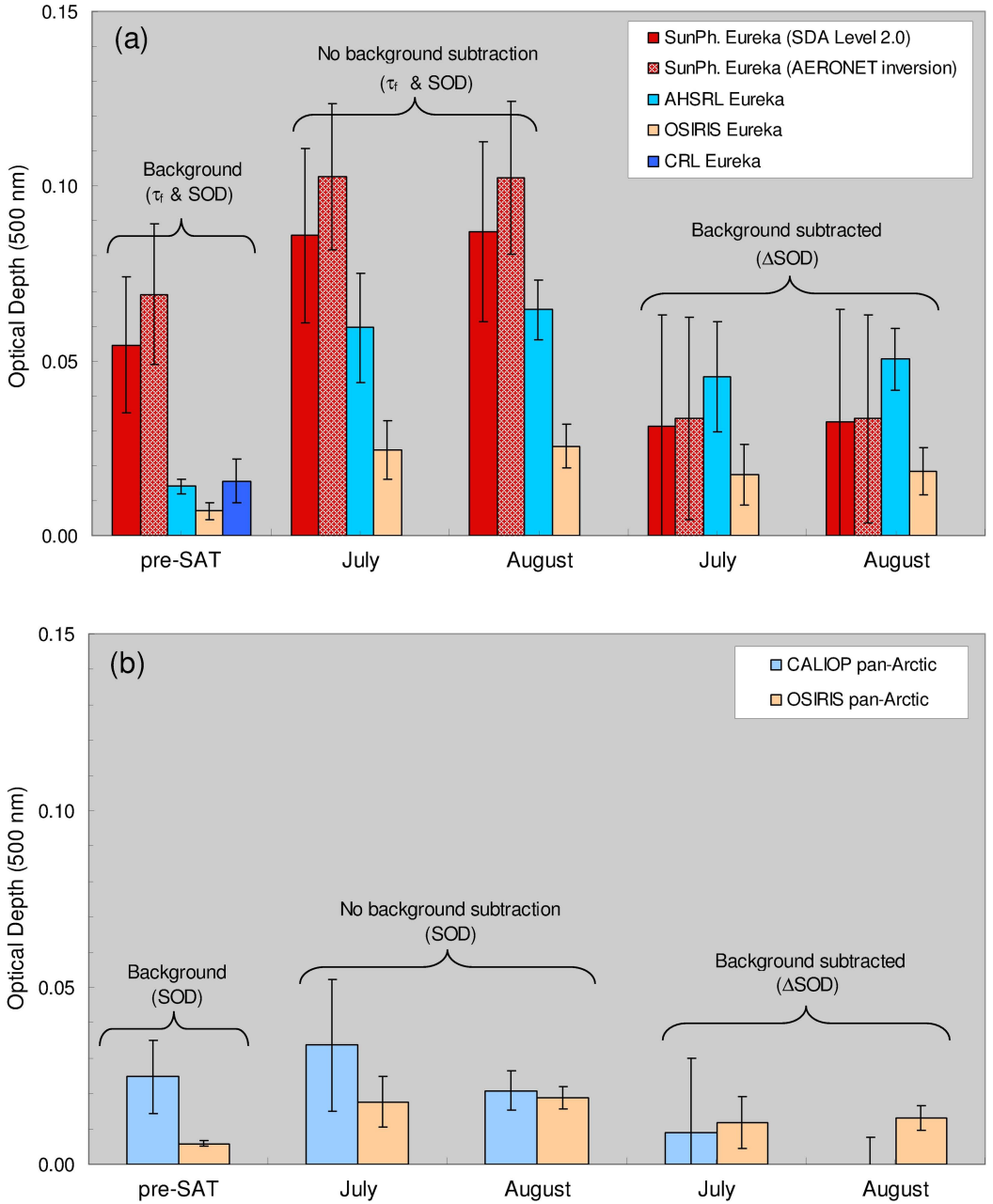
(a)
SunPh. Eureka (SDA Level 2.0)
SunPh. Eureka (AERONET inversion)
AHSRL Eureka
OSIRIS Eureka
CRL Eureka
Optical Depth (500 nm)
0.15
0.10
0.05
0.00
Background
(τf & SOD)
No background subtraction
(τf & SOD)
Background subtracted
(ΔSOD)
pre-SAT
July
August
July
August
(b)
CALIOP pan-Arctic
OSIRIS pan-Arctic
Optical Depth (500 nm)
0.15
0.10
0.05
0.00
Background
(SOD)
No background subtraction
(SOD)
Background subtracted
(ΔSOD)
pre-SAT
July
August
July
August

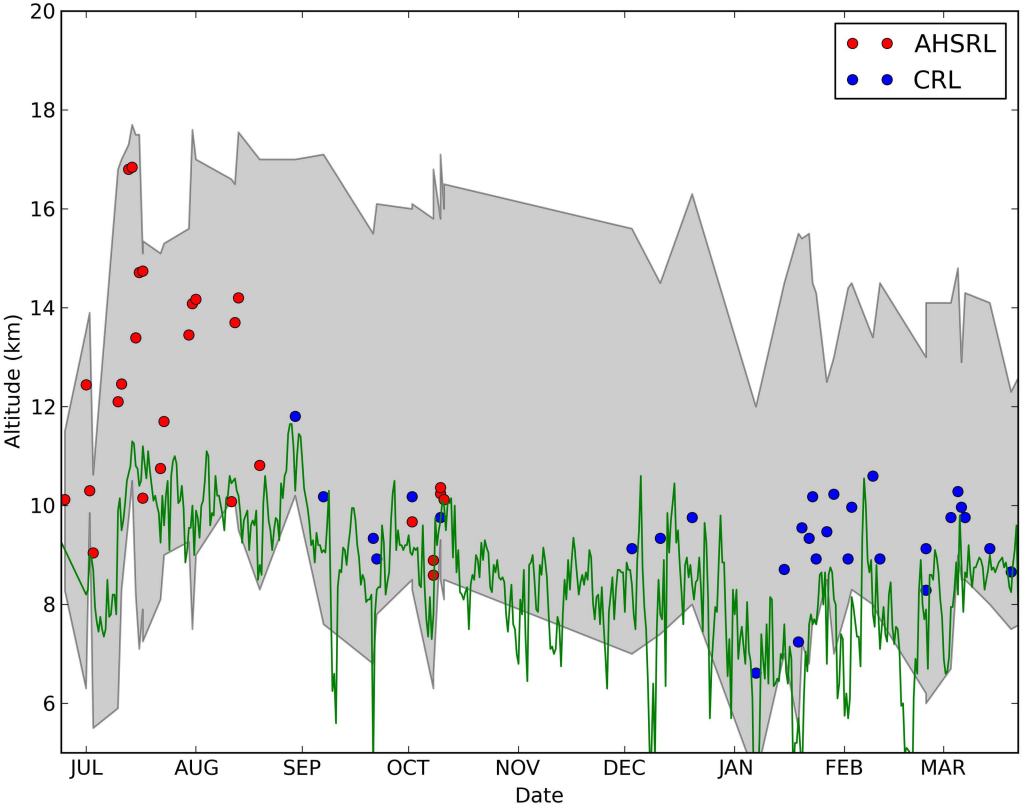
AHSRL
CRL
Altitude (km)
20
18
16
14
12
10
8
6
JUL
AUG
SEP
OCT
NOV
DEC
JAN
FEB
MAR
Date

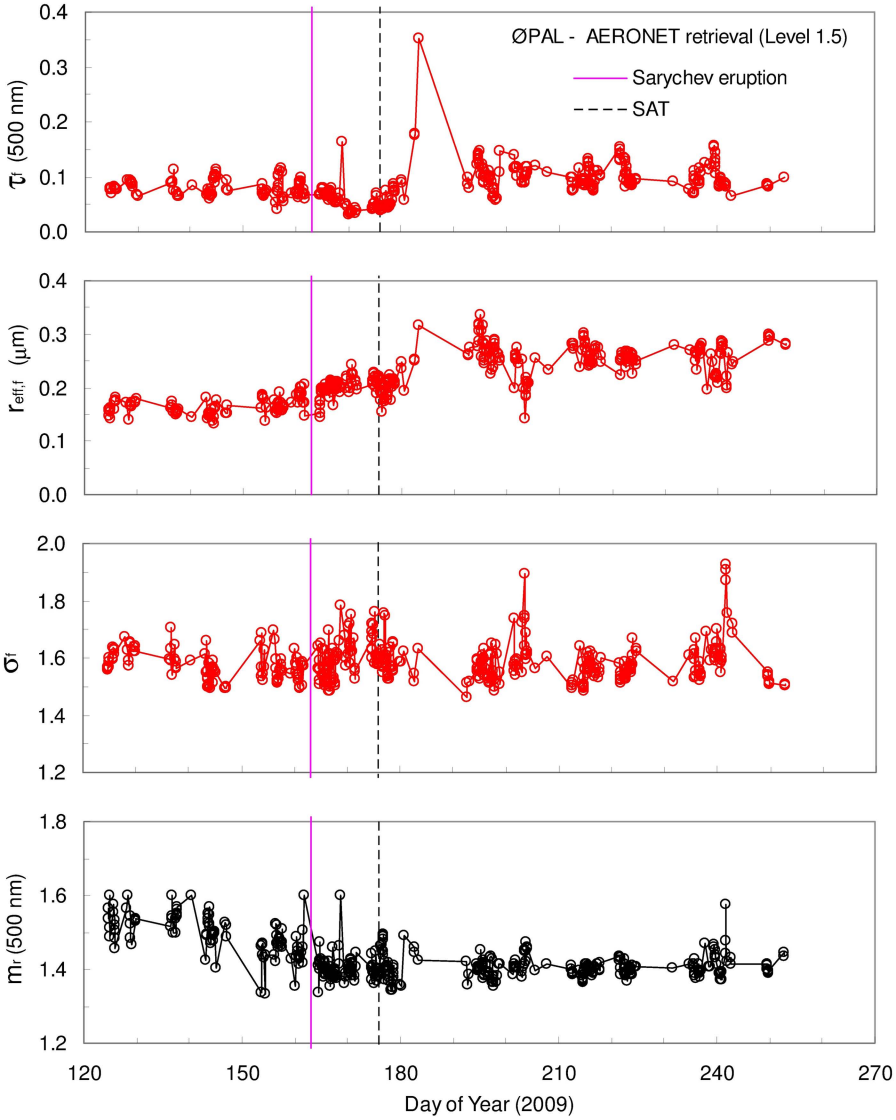
ØPAL - AERONET retrieval (Level 1.5)
Sarychev eruption
SAT
τf (500 nm)
reff,f (μm)
σf
mr (500 nm)
Day of Year (2009)

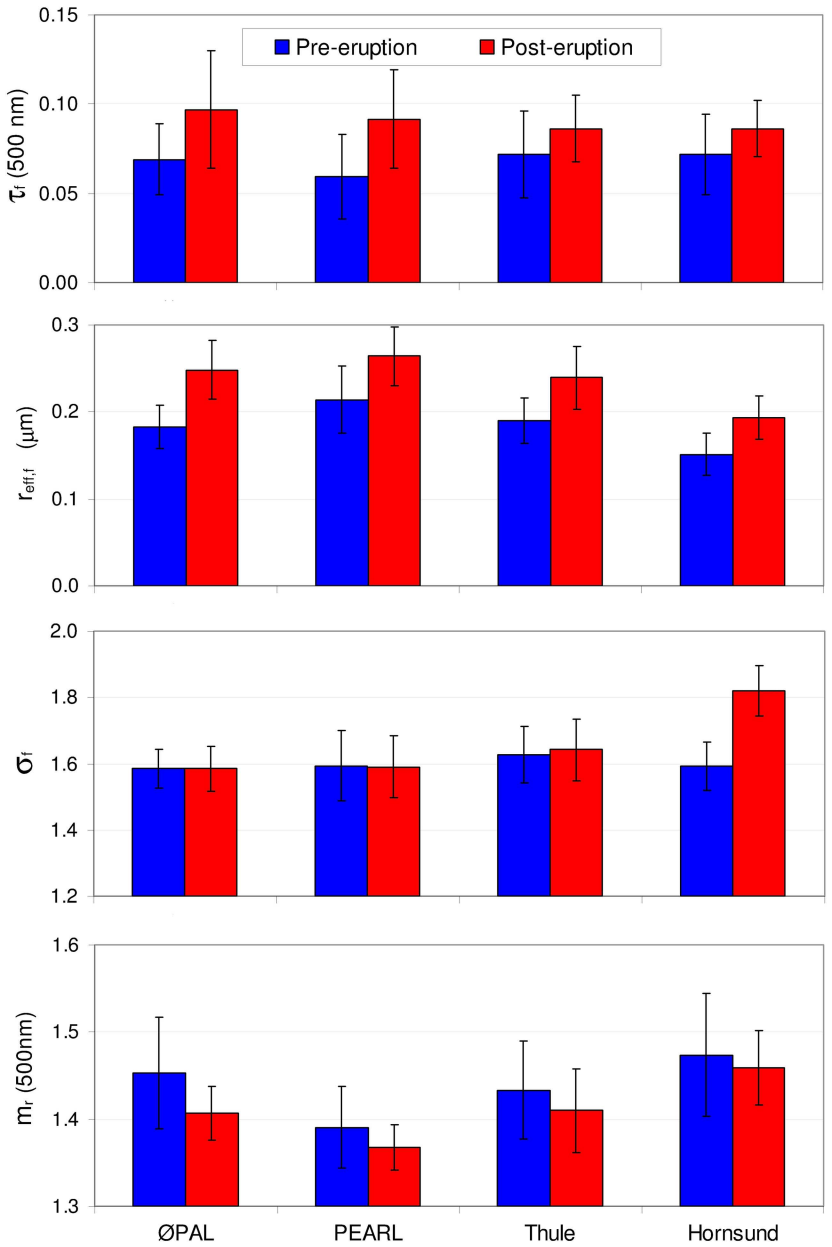
Pre-eruption
Post-eruption
τ_f (500 nm)
0.15
0.10
0.05
0.00
$r_{eff,f}$ (µm)
0.3
0.2
0.1
0.0
σ_f
2.0
1.8
1.6
1.4
1.2
m_r (500nm)
1.6
1.5
1.4
1.3
ØPAL
PEARL
Thule
Hornsund

(a)

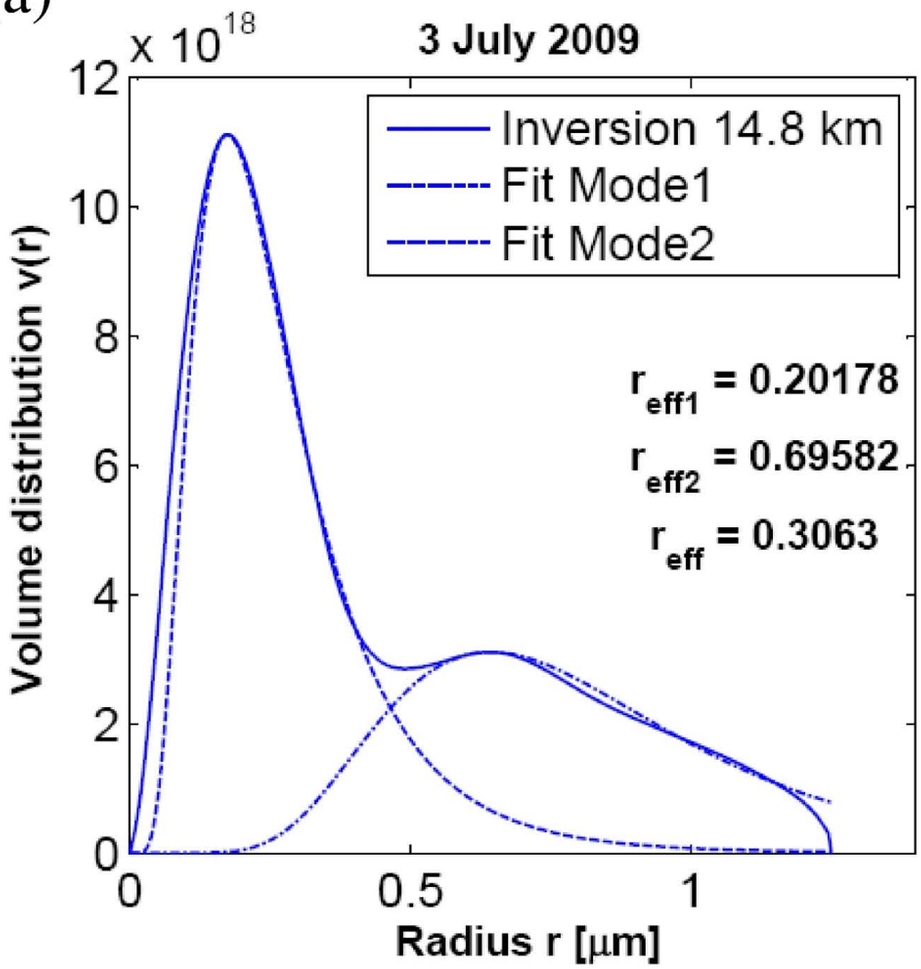
x 10^18
3 July 2009
Inversion 14.8 km
Fit Mode1
Fit Mode2
r_eff1 = 0.20178
r_eff2 = 0.69582
r_eff = 0.3063
Volume distribution v(r)
Radius r [μm]

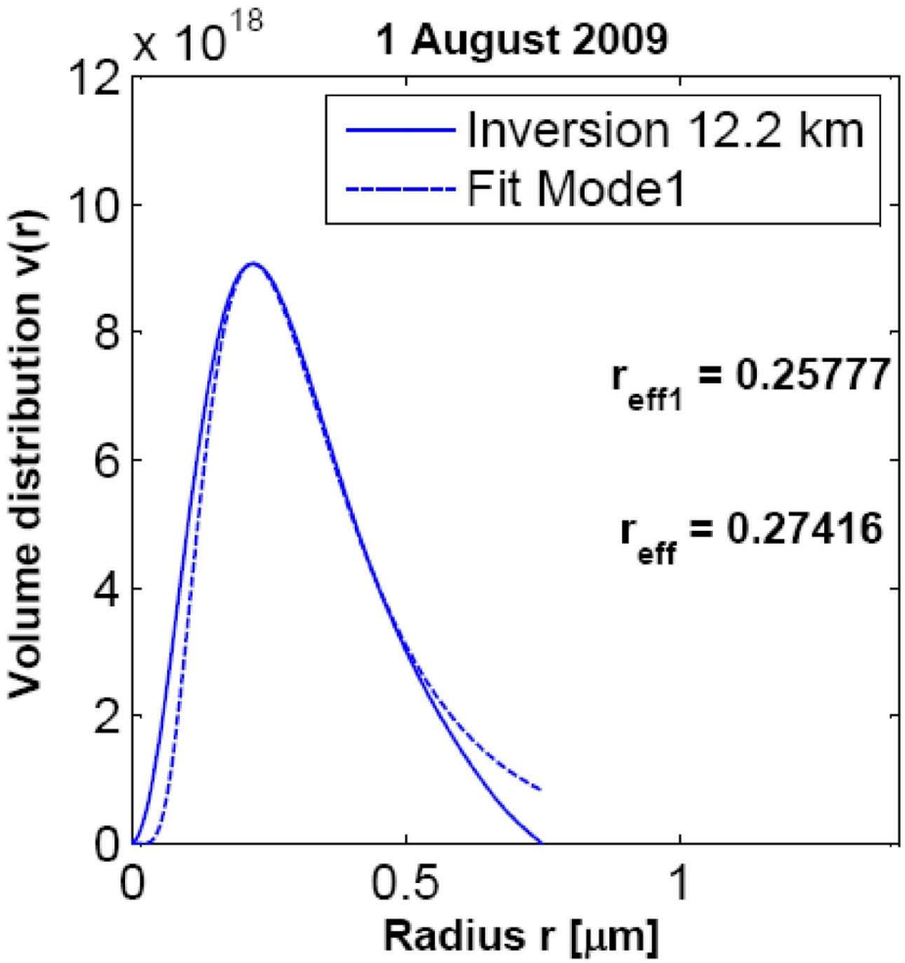
x 10^18
1 August 2009
Inversion 12.2 km
Fit Mode1
r_eff1 = 0.25777
r_eff = 0.27416
Volume distribution v(r)
Radius r [μm]

(b)

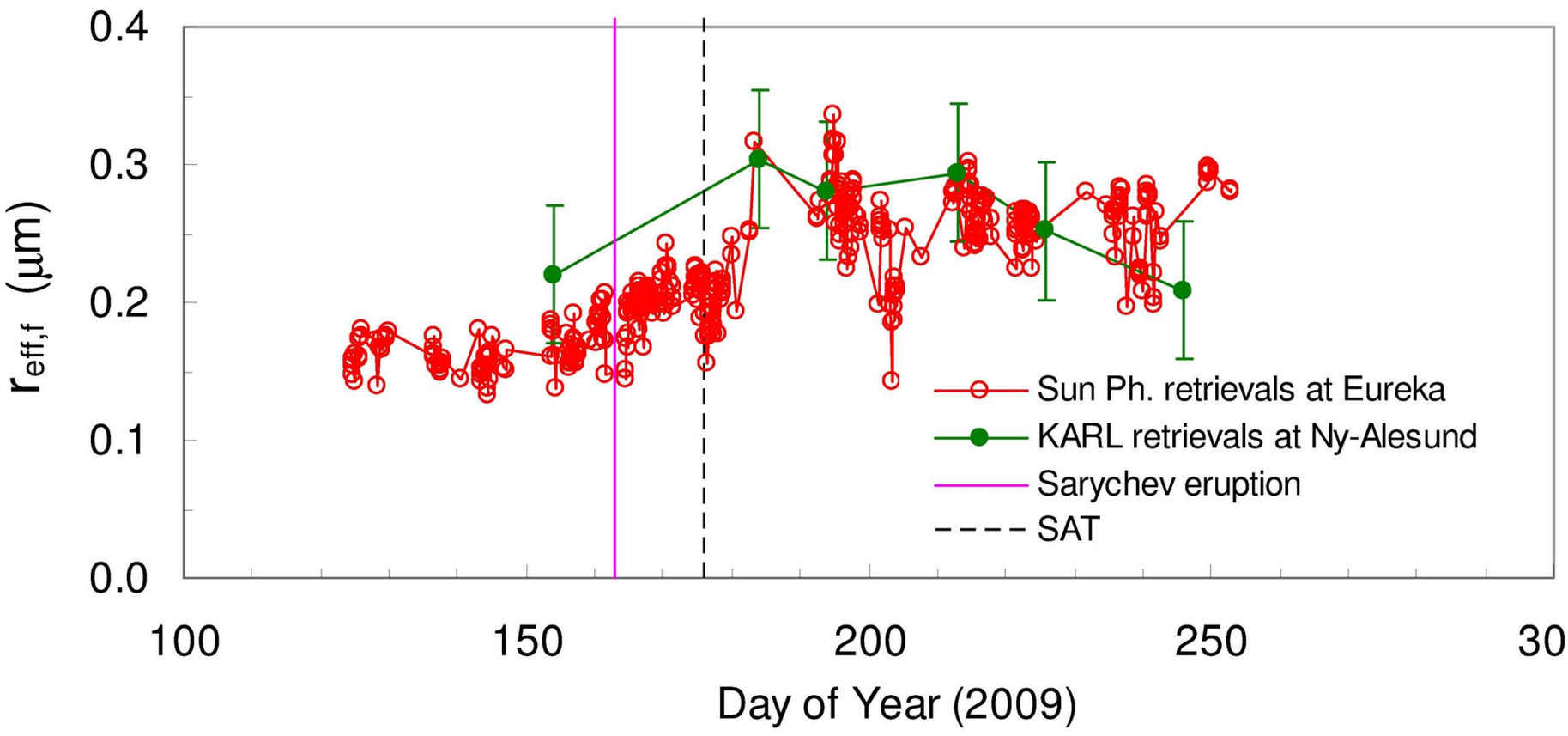
r_eff,f (μm)
Sun Ph. retrievals at Eureka
KARL retrievals at Ny-Alesund
Sarychev eruption
SAT
Day of Year (2009)